Broadband noise prediction for aerofoils with a serrated trailing edge based on Amiet's theory

Matthieu B. R. Gelot & Jae Wook Kim

Institute of Sound and Vibration Research, University of Southampton

Southampton, SO17 1BJ, United Kingdom

Abstract

Trailing-edge serrations are used as means to reduce aerofoil broadband self-noise in various industrial applications. However, a reliable prediction of the reduced noise level has not been established to date. In this paper, the authors suggest that Amiet's theory can be used to accurately predict the sound radiated from serrated trailing edges. A plausible explanation as to how the classical theory, originally derived from non-serrated (straight) trailing edges, also works for the serrated trailing edges is provided. Besides, the authors propose a directivity correction to the Amiet's original model to account for realistic aerofoil geometry. The directivity correction provides a significantly improved prediction of the noise level in the upstream and downstream directions for both serrated and baseline trailing edge cases. This study is based on wall-resolved large-eddy simulations of Joukowski aerofoils with multiple serration geometries and in different flow conditions.

Keywords: Trailing-edge noise; Computational aeroacoustics

1. Introduction

Aerodynamic noise is critical to many industrial applications such as wind turbines. It is well-known that aerodynamic noise generated by aerofoils is of numerous natures [1]. Trailing-edge (TE) noise results from the scattering, at the aerofoil trailing edge, of surface pressure fluctuations convecting within the turbulent boundary layer. It has been shown by Oerlemans [2] that TE noise constitutes the main source of aerodynamic sound coming from a wind turbine and it has been investigated extensively through a wide range of approaches whether it be analytical [3–12], experimental [13–15] or computational [16, 17].

The use of a serrated trailing edge (STE) as a means of broadband TE noise reduction has been investigated for decades by numerous authors. TE serrations can refer to all sorts of spanwise-varying TE geometries. The most common is the sawtooth geometry since it provides satisfying noise abatement performances and is easily applicable to industrial scale but different shapes have been tested in the literature [18]. Multiple experimental studies have been carried out over the last thirty years. Dassen et al. [19] conducted some experiments on NACA aerofoils and flat plates and showed that the expected noise reduction from STE was around 5 dB which was later confirmed by Oerlemans et al. [20] who found a figure of 3.2 dB. Gruber et al. [21] investigated the noise reduction mechanisms and suggested that the serration amplitude (root to tip) should be longer than the turbulent boundary layer thickness to achieve a significant noise reduction. Moreau and Doolan [22] showed that the assumption of frozen turbulence usually employed in analytical models is incorrect and may explain the differences observed between measurements and

analytical predictions. Additionally, they suggested that the change of the hydrodynamic field near the serrations is more impactful on noise reduction than the change of diffraction properties. The most recent experiments [23–25] are based on PIV measurements and allow more detailed analysis of the flow features. The observations made by Avallone et al. [26] show that the turbulent intensity is higher at the root of sawtooth serrations than at the tip. Chong and Vathylakis [27] studied the viscid-inviscid interaction between the turbulent eddies and the oblique vortical structures along the TE. Computational methods have also been used to investigate STEs [28–30], however, no consensus has yet been found on the mechanism of STE broadband noise reduction. Thus, in contrast with the observations of Moreau and Doolan [22], all analytical models developed since the 1990s are based on a destructive phase interference mechanism. This includes the pioneering theoretical work of Howe [31] who published a Green's function-based analytical model for noise prediction of a semi-infinite serrated flat-plate. Lyu's and Ayton's [32–34] approaches are both based on the same governing equation but the Wiener-Hopf technique used in their most recent work considerably reduces the number of sums to compute in the model resulting in a much faster implementation. These models essentially spread a modulated single-point wall pressure fluctuations spectrum along the serrated edge and only account for cut-on modes. In other words, the source magnitude does not depend on the position along the edge.

This paper aims to develop an accurate prediction method of noise generated from serrated trailing edges. In this respect, high-resolution numerical simulations are carried out in order to obtain accurate wall pressure data near the aerofoil trailing edge. This highly accurate noise source data is then used in two different approaches namely, Ffowcs-Williams & Hawkings' [35] and Amiet's [3, 4], to calculate the radiated sound in the far-field. In this work, the authors take the Ffowcs-Williams & Hawkings (FW-H) solution as a reference solution and examine the accuracy of Amiet's solution relative to it. In this framework, the authors investigate the feasibility of using Amiet's model for the prediction of STE noise, which has not been reported to date. It is a controversial approach because Amiet's model was originally derived for a non-serrated (straight) trailing edge only. The authors also investigate a possible modification to Amiet's model to improve the accuracy of the STE noise prediction in a wide observer angle.

The paper is organised in the following order. Section 2 provides a case description as well as computational details. In Section 3, Amiet's noise prediction technique is used to predict the sound from LES data. Section 4 presents some numerical results explaining why this straight TE theory also works for STEs. Section 5 introduces a directivity correction factor to rectify the noise under-prediction in the upstream and downstream directions in Amiet's model. The capability of Amiet's model in the prediction of serrated trailing-edge noise reduction is exhibited in section 6 before conclusions are drawn in section 7.

2. Case description and computational methods

This section aims to exhibit the governing equations, numerical methods and computational details of the current study. In order to accurately capture the aerofoil surface pressure fluctuations over a wide range of frequencies, a high-resolution implicit large-eddy simulation (LES) approach based on a wavenumber-optimised discrete filter is used. The filter can be seen as an implicit subgrid-scale (SGS) model and thus, the scales which are smaller than the filter cut-off are dissipated. Garmann et al. [36] among others showed that an implicit LES is fully capable of capturing flow physics as accurately as the more conventional SGS model-based LES.

2.1. Governing equations and numerical schemes

In the present study, the computational fluid dynamics (CFD) is based on a wall-resolved large-eddy simulation (LES) by using the three-dimensional compressible Navier-Stokes equations. These equations are expressed in a conservative form, transformed onto a generalised coordinate system in the following fashion:

$$\frac{\partial}{\partial t}\left(\frac{\boldsymbol{Q}}{J}\right)+\frac{\partial}{\partial \xi_i}\left(\frac{\boldsymbol{E}_j-Re_\infty^{-1}M_\infty \boldsymbol{F}_j}{J}\frac{\partial \xi_i}{\partial x_j}\right)=-\frac{a_\infty}{L_c}\frac{\boldsymbol{S}}{J}, \tag{1}$$

where the indices $i=1,2,3$ and $j=1,2,3$ denote the three dimensions; a_∞ is the ambient speed of sound and $\boldsymbol{S}$ is a source term. The vectors of the conservative variables, inviscid and viscous fluxes are given by

$$\left.\begin{aligned}\boldsymbol{Q}&=[\rho,\rho u,\rho v,\rho w,\rho e_\mathrm{t}]^T,\\ \boldsymbol{E}_j&=[\rho u_j,(\rho u u_j+\delta_{1j}p),(\rho v u_j+\delta_{2j}p),(\rho w u_j+\delta_{3j}p),(\rho e_\mathrm{t}+p)u_j]^T,\\ \boldsymbol{F}_j&=[0,\tau_{1j},\tau_{2j},\tau_{3j},u_i\tau_{ji}+q_j]^T,\end{aligned}\right\} \tag{2}$$

with the stress tensor and heat flux vector reading as

$$\tau_{ij}=\mu\left(\frac{\partial u_i}{\partial x_j}+\frac{\partial u_j}{\partial x_i}-\frac{2}{3}\delta_{ij}\frac{\partial u_i}{\partial x_i}\right),\quad q_j=\frac{\mu}{(\gamma-1)Pr}\frac{\partial T}{\partial x_j}, \tag{3}$$

where $\xi_i=\{\xi,\eta,\zeta\}$ are the generalised coordinates, $x_j=\{x,y,z\}$ are the Cartesian coordinates, δ_{ij} is the Kronecker delta, $u_j=\{u,v,w\}$, $e_\mathrm{t}=p/[(\gamma-1)\rho]+u_ju_j/2$ and $\gamma=1.4$ for air. The local dynamic viscosity μ is calculated by using Sutherland's law [37]. The free-stream Mach and Reynolds numbers are defined as $M_\infty=u_\infty/a_\infty$ and $Re_\infty=\rho_\infty u_\infty L_c/\mu_\infty$. The governing equations are non-dimensionalised based on the aerofoil chord length L_c for length scales, the ambient speed of sound a_∞ for velocities, L_c/a_∞ for time scales and $\rho_\infty a_\infty^2$ for pressures. Temperature, density and dynamic viscosity are normalised by their respective ambient values: T_∞, ρ_∞ and μ_∞. For the sake of clarity, figure labels and legends explicitly show the normalisation. For example, the PSD of wall pressure fluctuations non-dimensionalised by the ambient pressure is written S_{qq}/p_∞^2. In the current configuration, ξ, η and ζ are aligned in the streamwise, wall-normal and spanwise directions, respectively. The Jacobian determinant of the coordinate transformation (from Cartesian to generalised) is given by $J^{-1}=|\partial(x,y,z)/\partial(\xi,\eta,\zeta)|$.

The implicit LES uses high-order accurate schemes. The spatial derivatives are computed using an optimised pentadiagonal compact finite difference scheme which is fourth-order accurate up to the boundaries [38]. The explicit time marching makes use of a matching fourth-order Runge-Kutta scheme with a Courant-Friedrichs-Lewy (CFL) number of 1.0. A sixth-order pentadiagonal compact filter with a normalised cut-off wavenumber of 0.85π is used alongside [39]. It dissipates unresolved sub-grid scales and ensures the numerical stability. The computation is parallelised based on a message passing interface (MPI). The MPI parallelisation of the compact scheme and filter is implemented by using the quasi-disjoint matrix system proposed by Kim [40]. All simulations are carried out in either the UK national supercomputer ARCHER or in IRIDIS 5 cluster at the University of Southampton. Depending on which computing facility is used, the computational domain is decomposed and distributed over 3840 or 512 processor cores for ARCHER and IRIDIS 5 respectively.

2.2. Computational domain, grid and boundary conditions

The current simulations are based on cambered Joukowski aerofoils with different thickness. Table 1 gathers all the cases explored in this study. Two different Joukowski aerofoils are studied: the first one has a thickness of 10% and camber of 5.15% (relative to the chord); the second one has a thickness of 12% and camber of 4.25% (Fig. 1). The reason behind selecting Joukowski aerofoils is that it has a sharp trailing edge with matching trailing-edge slopes on pressure and suction sides. Consequently, it can accommodate flat-plate serrations add-ons without any modification of the aerofoil profile. The flow set-up is carefully chosen for each aerofoil to avoid a strong recirculation in the transitional region which could engender undesirable tonal noise for the current broadband noise investigation. This pre-simulation check-up is performed using XFoil [41]. The leading edge lies on the z-axis and the trailing edge is located at $(x, y)/L_c = (1, 0)$ in the baseline trailing-edge (BTE) case. Three different serrated trailing-edge (STE) geometries are studied (Table 1). The aspect ratio is defined by the streamwise length divided by the spanwise wavelength of the serration. The serrations extend from the baseline geometry. The local chord length is the same as the baseline case at the roots of the serrations and it lengthens at the tips. The spanwise domain size is initially set to 5% of the chord length ($L_s = 0.05L_c$) of the baseline aerofoil. This particular length of $0.05L_c$ is also used as the wavelength of the serrations. The aerofoil chord is aligned with the x-axis.

#	Case	Re_∞	M_∞	α	AR	L_s/L_c
1	JK10-BTE	3×10^5	0.3	6.5°	0.00	0.05
2	JK10-STE0.75	3×10^5	0.3	6.5°	0.75	0.05
3	JK10-STE1.00	3×10^5	0.3	6.5°	1.00	0.05
4	JK10-STE1.25	3×10^5	0.3	6.5°	1.25	0.05
5	JK10-BTE-ext.	3×10^5	0.3	6.5°	0.00	0.10
6	JK10-STE0.75-ext.	3×10^5	0.3	6.5°	0.75	0.10
7	JK10-STE1.00-ext.	3×10^5	0.3	6.5°	1.00	0.10
8	JK10-STE1.25-ext.	3×10^5	0.3	6.5°	1.25	0.10
9	JK12-BTE	5×10^5	0.2	6.0°	0.00	0.05
10	JK12-STE1.00	5×10^5	0.2	6.0°	1.00	0.05
11	JK12-STE1.25	5×10^5	0.2	6.0°	1.25	0.05

Table 1: The current simulation cases for various flow conditions and STE geometries; JKXX stands for a Joukowski aerofoil of XX% thickness; BTE stands for baseline trailing-edge; STEYYY stands for serrated trailing-edge of aspect ratio YYY; -ext. refers to extended span cases; Re_∞ is the Reynolds number; M_∞ is the Mach number; α is the angle of attack; AR defines the aspect ratio of the sawtooth serrations and L_s/L_c is the span-to-chord ratio.

A structured H-type topology is utilised for all grids. Some examples of the grid meshes used in the current work are displayed in Fig. 2. The cells are progressively stretched from the aerofoil wall to the external boundaries with the smallest cells located on the aerofoil surface. A high level of grid resolution is kept in the near-field up to half a chord away from the aerofoil. In the STE cases, a finer grid spacing is used near the sharp corners and a matching distribution is used in the BTE case for consistency. The tips and roots of the serrations are gently rounded (with a radius of 3% of the span length): this is to preserve the sharp character of the serrations and to maintain a smooth mesh with continuous

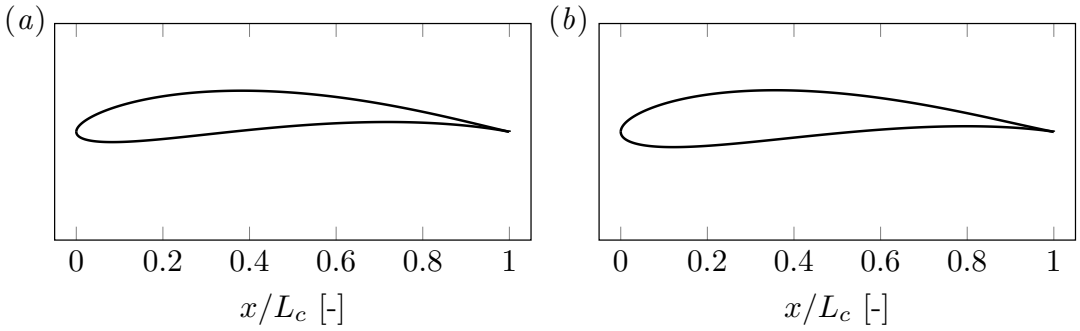

Figure 1: Joukowski JK10 (10% thickness; 5.15% camber) and JK12 (12% thickness; 4.25% camber) aerofoil profiles.

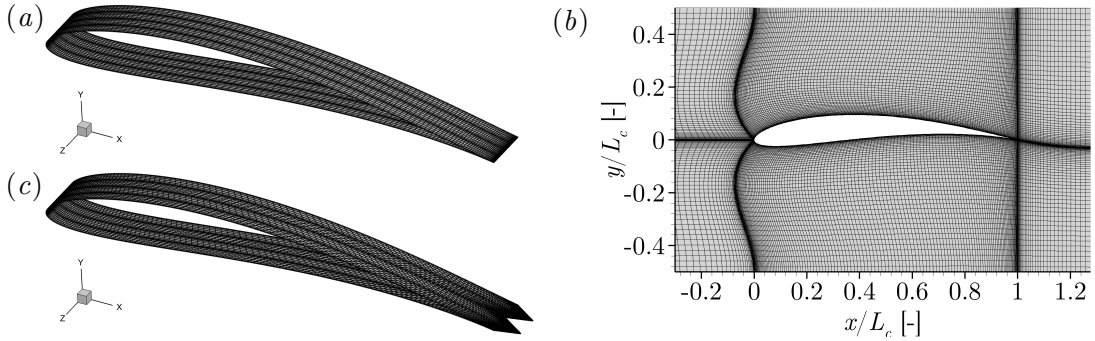

Figure 2: (a,c) A bird's eye view of the surface mesh for the JK10-BTE and JK10-STE1.00 aerofoils showing a span of 10% chord and (b) a cross-sectional view of the interior mesh of the BTE case. The pictures only show 25% of total cell count for display purposes.

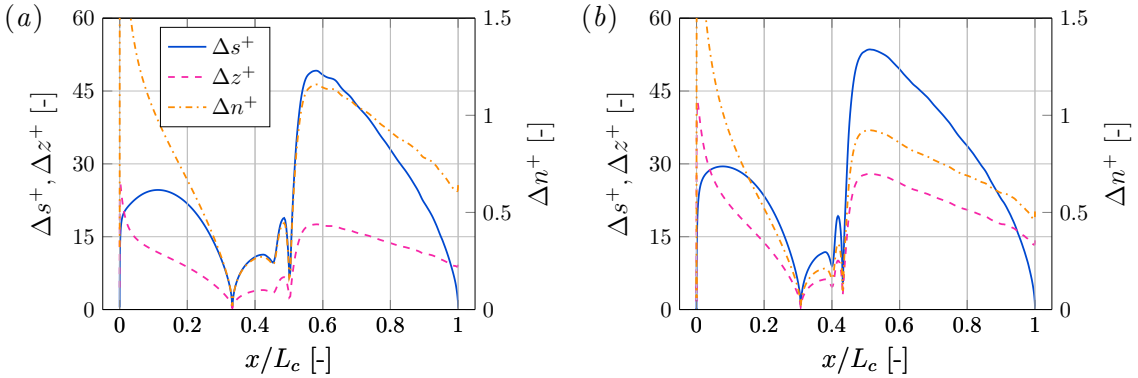

Figure 3: Wall-unit grid spacings used on the suction side for (a) the JK10-BTE case and (b) the JK12-BTE case where Δs^+ is the streamwise curvilinear spacing, Δz^+ is the spanwise spacing and Δn^+ is the wall-normal spacing.

derivatives. In the JK10 case, the number of grid cells are $(N_\xi, N_\eta, N_\zeta) = (960, 480, 50)$ in the streamwise, wall-normal and spanwise directions respectively. The overall cell count rounds up to 23 million in the case of $L_s = 0.05L_c$. The wall-unit grid sizes on the suction side are exhibited in Fig. 3. Georgiadis et al. [42] recommended that for LES simulations: $\Delta s^+ < 150$, $\Delta z^+ < 40$ and $\Delta n^+ < 1$ in the turbulent region; where $\Delta s^+, \Delta n^+$ and Δz^+ are the body-fitted streamwise, wall-normal and spanwise wall-unit grid spacings, respectively. The grid sizes resulting from the present simulations are within the brackets apart from Δn^+ in the JK10 case that exhibits a short region over 1 after the transition. However,

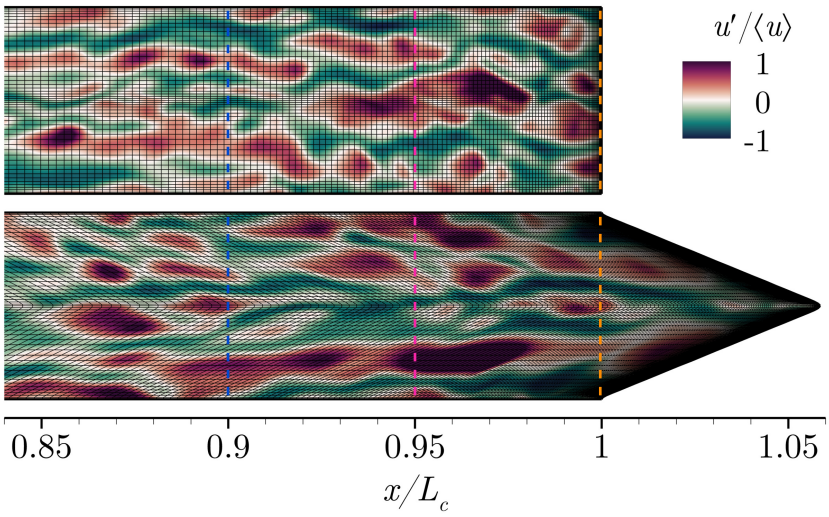

Figure 4: Snapshot of the streamwise velocity streaks in near-wall turbulent flow at $y^+ = 6$ from the wall (at the TE) for the JK10-BTE (top) and the JK10-STE1.25 (bottom) cases. The coloured lines depict the data extraction performed to plot Fig. 5.

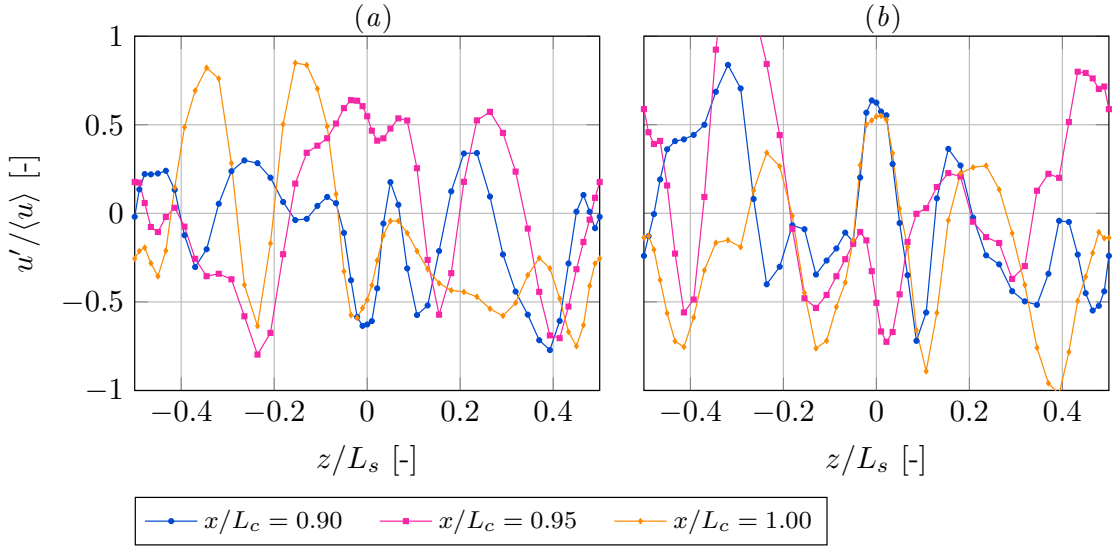

Figure 5: Distribution of the normalised streamwise velocity fluctuations along the spanwise direction at three different streamwise location $x/L_c = 0.90, 0.95, 1.00$ near the TE in (a) the JK10-BTE and (b) the JK10-STE1.25 cases. The markers represent the grid points.

this is not critical since the LES simulation is performed using high-order accurate schemes and it does not affect the accuracy of the results. The spanwise grid resolution is further investigated with Fig. 4 which displays a snapshot of the streamwise velocity streaks in the near-wall turbulent flow. Following the work of Chernyshenko and Baig [43], the streaks are plotted at $y^+ = 6$ (value taken at the TE). Two cases are presented: JK10-BTE and JK10-STE1.25. The mesh is also displayed in order to appreciate the resolution of the streaks. This resolution is better represented in Fig. 5 where the spanwise distribution of the streamwise velocity fluctuations – normalised by the time averaged streamwise velocity – is plotted at three different locations. The figure shows that a streak spanwise period is approximately resolved by 10 grid points.

The horizontal and vertical far-field boundaries are treated with general characteristic-

based non-reflecting boundary conditions (GCBCs) [44] to inhibit spurious reflections from outgoing sound waves. Furthermore, a sponge layer [45, 46] is introduced via the source term $\boldsymbol{S}$ in Eq. (1) around the far-field boundaries to damp any disturbances and therefore enforce the mean flow conditions and absorb acoustic waves. A representation of the domain with the sponge layer is given in Fig. 6. A no-slip iso-thermal wall boundary condition is applied on the aerofoil surface and a periodic boundary condition is applied across the spanwise boundaries. For each case, the velocity is progressively ramped up from zero to the required inflow velocity over a period $ta_\infty/L_c = 5$ using a moving frame method. The resulting flow field is presented in Fig. 7 with the radiated sound represented by the divergence of velocity, the turbulent boundary layer depicted by Q-criterion=1 and flood by the velocity magnitude and the contour map of wall pressure fluctuations spectra.

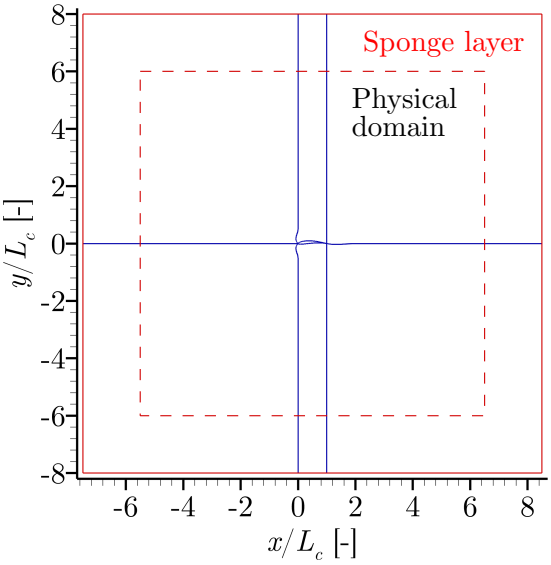

Figure 6: Representation of the computational domain: the region located inside the dashed contour is the physical domain and the area located between the solid and dashed lines is the sponge layer. The domain is decomposed in 6 blocks and their edges are coloured in blue.

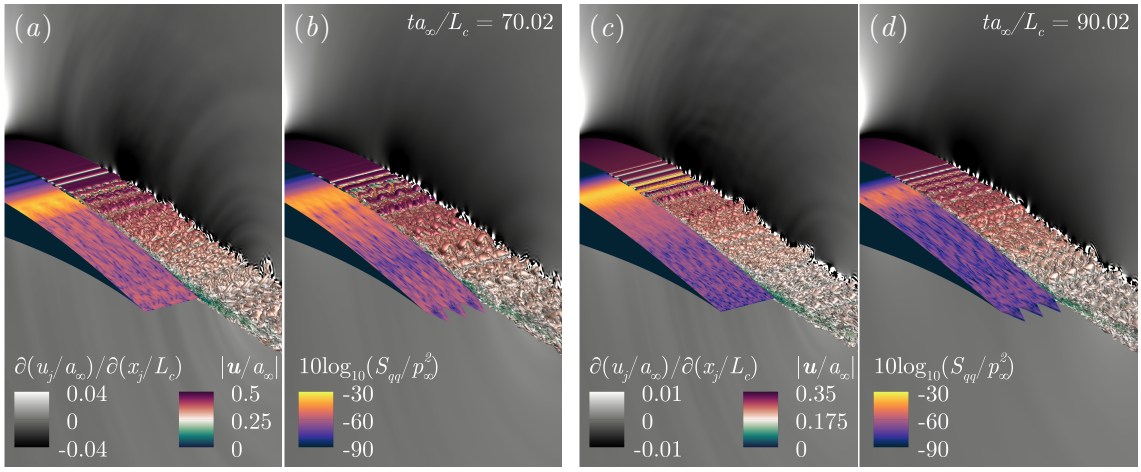

Figure 7: Three-dimensional visualisation of: the radiated sound represented by the divergence of velocity; the turbulent boundary layer depicted by Q-criterion=1 and flood by the velocity magnitude; the contour map of wall pressure fluctuations spectra. The cases displayed are (a) JK10-BTE; (b) JK10-STE1.25; (c) JK12-BTE and (d) JK12-STE1.25.

2.3. Validation of numerical simulations

Each simulation is run for at least $ta_\infty/L_c = 80$ time units in total to reach a fully developed numerical solution. Output for data processing is taken during the last 10 time units. The time history of the lift and drag coefficients (C_L and C_D) is recorded in Fig. 8 where the data extraction period is also specified for each case. In order to validate the numerical simulations, time- and spanwise-averaged profiles of the pressure and skin friction coefficients (C_p and C_f) are compared with the corresponding XFoil predictions in Fig. 9. The plots clearly show that the time-averaged solutions collapse with the XFoil

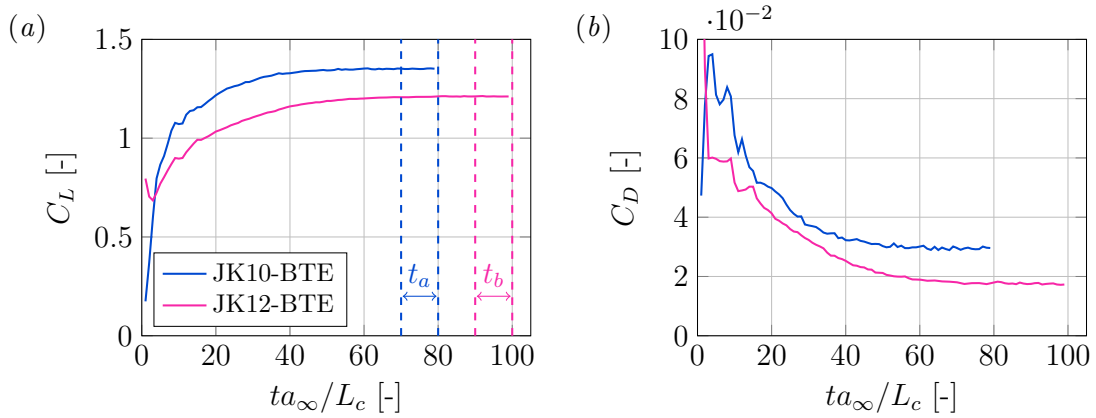

Figure 8: Time history of the lift and drag coefficients (C_L and C_D) for JK10-BTE and JK12-BTE cases. The time periods t_a and t_b correspond to the selected time periods for data extraction.

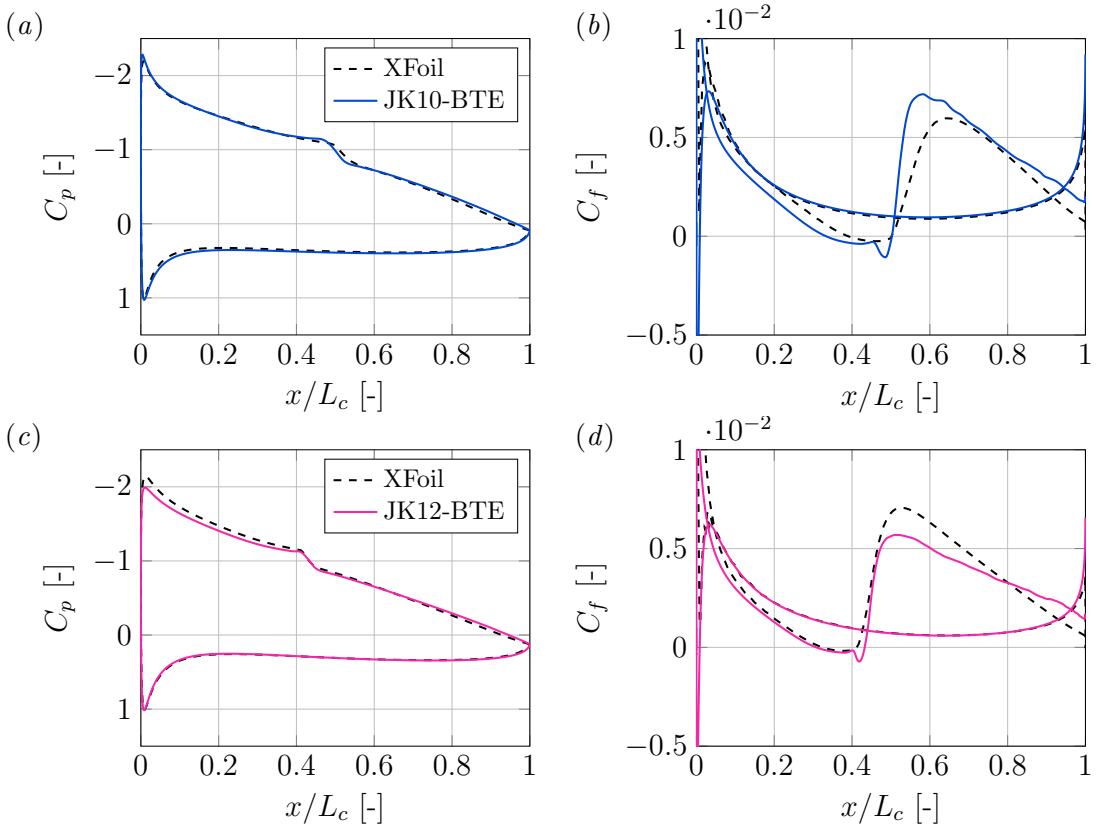

Figure 9: Time-averaged profiles of the pressure coefficient C_p and skin friction coefficient C_f for (a,b) the JK10 case and (c,d) the JK12 case. The baseline profiles are averaged in the spanwise direction.

predictions over the laminar region of the flow. A certain deviation in the skin friction is noticed in the turbulent region (suction side) and is perhaps associated with the difference between the two- and three-dimensional approaches. In order to further validate that the turbulent boundary layer is fully developed, the PSD of velocity fluctuations from a probe located in the $z = 0$ plane at $x/L_c = 0.95$ and at $y^+ = 150$ from the wall in the JK10-STE1.25 case is displayed in Fig. 10. The figure shows that the three components of velocity fluctuation align with the classical -5/3 slope for the inertial sub-range at high frequencies. Furthermore, the case has been run for an extra 50 time units to compare with the original extraction and the figure shows that the velocity spectra are analogous across the entire frequency range. This complements the findings of Fig. 8-9 and confirms that the case is already converged after $ta_\infty/L_c = 70$.

Furthermore, Fig. 11 shows a comparison of the loading noise from Eq. 4 produced in the far-field for the two different time intervals. A deviation of 5 dB is noticeable for $fL_c/a_\infty \simeq 1.5$, however the difference remains in a 1-2 dB bracket at other frequencies.

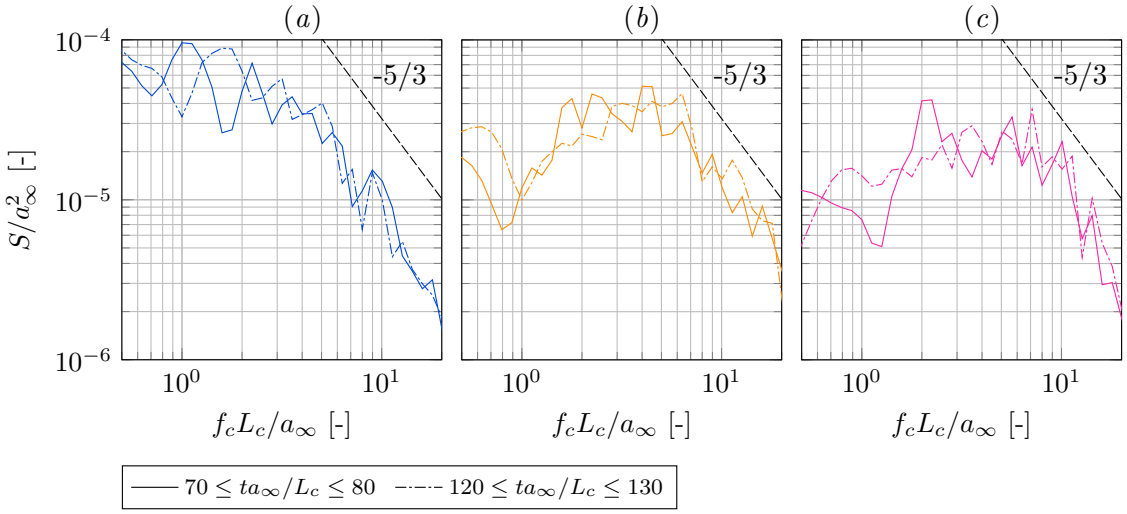

Figure 10: One-sixth octave PSD of velocity fluctuations from a probe located in the $z = 0$ plane at $x/L_c = 0.95$ and at $y^+ = 150$ from the wall in the JK10-STE1.25 case : (a) S_{uu}/a_∞^2, (b) S_{vv}/a_∞^2 and (c) S_{ww}/a_∞^2. The solid lines depict a signal extracted between $ta_\infty/L_c = 70$ and $ta_\infty/L_c = 80$ whereas the dashdotted lines depict a signal extracted after a longer running time between $ta_\infty/L_c = 120$ and $ta_\infty/L_c = 130$.

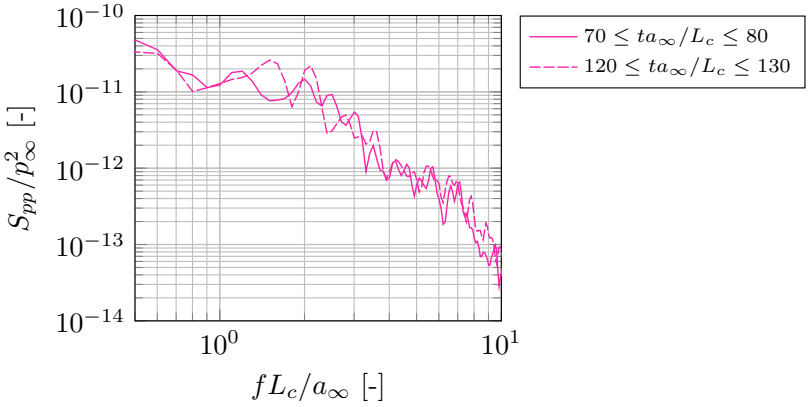

Figure 11: PSD of loading noise (Eq. 4) in the JK10-STE1.25 case over a circular arc $80° \leq \theta \leq 100°$ with radius $R/L_c = 10$ centred at $(x, y, z)/L_c$=(1,0,0). The plot compares two extraction time intervals.

Hence, the time interval has little impact on the noise calculation and the earlier interval is satisfactory enough to perform acoustics computations.

A span length study is proposed in Appendix A to investigate the impact of the span extent on the far-field sound. A difference between 5% and 10% spans is noticeable at lower frequencies and this is likely attributed to the capability of the larger span case to resolve larger spanwise structures. However, the capability of the method exposed in this paper is unchanged as long as the same source is used for FW-H and Amiet's calculations. The appendix also includes a time period study to explore the influence of the time period on the low-frequency content.

2.4. Calculation of the acoustic field

In the present paper, a time-domain Ffowcs-Williams & Hawkings [35] approach is adopted to calculate the acoustic solutions in the far-field. The numerical implementation of FW-H is based on Farassat's "formulation 1A" [47]. Since the monopole and quadrupole contributions are irrelevant to the current study, the loading noise is solely considered and the following equation is used:

$$4\pi p' = \int_S \left[\frac{\dot{p}\cos\theta}{a_\infty r(1-M_r)^2} + \frac{p(\cos\theta - M_i n_i)}{r^2(1-M_r)^2} + \frac{(M_r - M_\infty^2)(p\cos\theta + \rho_\infty a_\infty u_i n_i)}{r^2(1-M_r)^3} \right]_{ret} \mathrm{d}S, \tag{4}$$

where dotted variables indicate time derivatives; *ret* specifies that the variables within the brackets are taken at the retarded time $\tau = t - r/a_\infty$; $M_\infty = |\boldsymbol{M}|$ is the Mach number and r is the effective acoustic distance computed from an extension of the Garrick triangle to two-dimensional mean flow velocity,

$$r = \frac{M_x d_x + M_y d_y + [(M_x d_x + M_y d_y)^2 + (1 - M_x^2 - M_y^2)(d_x^2 + d_y^2 + d_z^2)]^{-1/2}}{1 - M_x^2 - M_y^2}, \tag{5}$$

where $(M_x, M_y) = (M_\infty \cos\alpha, M_\infty \sin\alpha)$ and $(d_x, d_y, d_z) = (x_o - x_s, y_o - y_s, z_o - z_s)$ where o and s refer to observer and source respectively. $M_r = \boldsymbol{M} \cdot \hat{\boldsymbol{r}}$ where $\hat{\boldsymbol{r}}$ is the unit length effective acoustic vector. The local radiation angle θ is determined by $\cos\theta = \boldsymbol{n} \cdot \hat{\boldsymbol{r}}$ with $\boldsymbol{n}$ the local outward surface unit normal vector. A numerical validation of this implementation was proposed by Turner and Kim [48]. Appropriate radii and observer angles are to be specified when required. Since the LES simulations use periodic boundary conditions in the spanwise direction, this needs to be reflected in the FW-H calculation as

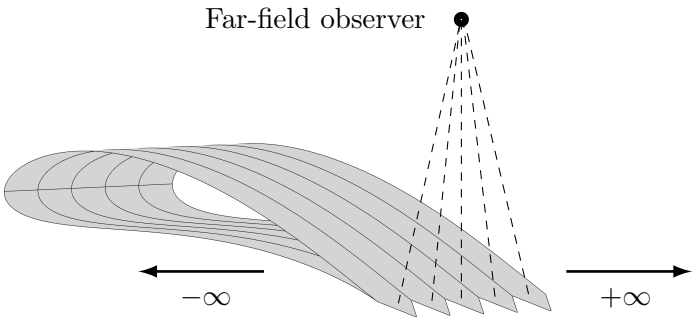

Figure 12: Schematic diagram of the computation of FW-H by juxtaposing multiple spans. $N_{span} = 5$ on the diagram but real calculations involve hundreds.

well and this is the reason why multiple spans are repeated as depicted in Fig. 12. The number of spans is noted N_{span}. In the authors' experience, convergence is already reached when $N_{span}L_s = 20L_c$ and this is the parameter used in the present study. Moreover, for the range of frequencies ($0.5 < fL_c/a_\infty < 10$) and for an observer lying 100 chords away from the source ($R = 100L_c$), $fR/a_\infty \gg 1$ so the observer truly lies in the acoustic far-field.

2.5. Definition of variables for spectral analysis

Data processing is performed for each completed simulation. In this aeroacoustics study, the main property of interest is the power spectral density (PSD) function of pressure fluctuations on the aerofoil wall and in the far-field. The pressure fluctuations read

$$p'(\boldsymbol{x}, t) = p(\boldsymbol{x}, t) - \overline{p}(\boldsymbol{x}), \tag{6}$$

where $\overline{p}$ is the time-averaged pressure. The wall pressure jump is defined by the difference between the pressure fluctuations on the suction and pressure sides:

$$\Delta p'_w(x, z, t) = p'(x, y_{ss}, z, t) - p'(x, y_{ps}, z, t), \tag{7}$$

where ss and ps designate the suction and pressure sides respectively. According to the definitions given by Goldstein [49], the frequency-based one-sided PSD functions of the pressure fluctuations are determined by

$$\begin{aligned} S_{pp}(\boldsymbol{x}, f) &= \lim_{T\to\infty} \frac{P(\boldsymbol{x}, f, T)P^*(\boldsymbol{x}, f, T)}{T}, \\ S_{qq}(\boldsymbol{x}, f) &= \lim_{T\to\infty} \frac{\Delta P_w(\boldsymbol{x}, f, T)\Delta P_w^*(\boldsymbol{x}, f, T)}{T}, \end{aligned} \tag{8}$$

where * denotes a complex conjugate, T represents the half-length of the time signals, P and ΔP_w are approximate Fourier transforms of p' and $\Delta p'_w$ based on the following definitions

$$\begin{aligned} P(\boldsymbol{x}, f, T) &= \int_{-T}^{T} p'(\boldsymbol{x}, t) e^{-2\pi \mathrm{i} f t}\, \mathrm{d}t, \\ \Delta P_w(\boldsymbol{x}, f, T) &= \int_{-T}^{T} \Delta p'_w(\boldsymbol{x}, t) e^{-2\pi \mathrm{i} f t}\, \mathrm{d}t. \end{aligned} \tag{9}$$

S_{pp} and S_{qq} are used for far-field acoustic pressure spectra and wall pressure jump spectra respectively. The wall-pressure coherence between two points $\boldsymbol{x}_1$ and $\boldsymbol{x}_2$ is defined by

$$\gamma_c^2(\boldsymbol{x}_1, \boldsymbol{x}_2, f) = \frac{|S_{qq}(\boldsymbol{x}_1, \boldsymbol{x}_2, f)|^2}{S_{qq}(\boldsymbol{x}_1, f) S_{qq}(\boldsymbol{x}_2, f)}, \tag{10}$$

where $S_{qq}(\boldsymbol{x}_1, \boldsymbol{x}_2, f)$ is the cross power spectral density defined by

$$S_{qq}(\boldsymbol{x}_1, \boldsymbol{x}_2, f) = \lim_{T\to\infty} \frac{\Delta P_w(\boldsymbol{x}_1, f, T)\Delta P_w^*(\boldsymbol{x}_2, f, T)}{T} \tag{11}$$

2.6. Sound pressure level

The sound pressure level (SPL) spectrum in dB per non-dimensional frequency unit is expressed with the PSD of far-field pressure fluctuations as a function of frequency

$$\mathrm{SPL}(f) = 10 \log_{10} \left[\frac{S_{pp}(f)}{p_0^2} \right] \tag{12}$$

where $p_0 = 2 \times 10^{-5}$ Pa is the acoustic reference pressure. The overall sound pressure level (OASPL) is obtained by integrating the PSD over all frequencies as follows

$$\mathrm{OASPL} = 10 \log_{10} \left[\frac{1}{p_0^2} \int_{-\infty}^{\infty} S_{pp}(f) \, \mathrm{d}f \right] \tag{13}$$

In practice, the integration is only performed over a reliable frequency range which depends on the sampling frequency and the length of the time signal. In the present simulations, the most reliable low frequency is $fL_c/a_\infty = 0.5$ and the most reliable high frequency is $fL_c/a_\infty = 10$.

3. Amiet's noise prediction model for serrated trailing edges

The authors explored a new use of Amiet's [3, 4] noise prediction model to predict the noise for serrated trailing-edges. A description of the method is given before showing remarkable outcomes.

3.1. Description of the model

The principle of the present usage of Amiet's model is relatively simple. First, wall pressure fluctuations time signals are extracted along a path line at a fixed distance from the actual TE (Fig. 13) and a spectrum is computed for each point providing a frequency-span PSD distribution $S_{qq}(z, \omega)$ where $\omega = 2\pi f$ is the angular frequency and z is the spanwise coordinate.

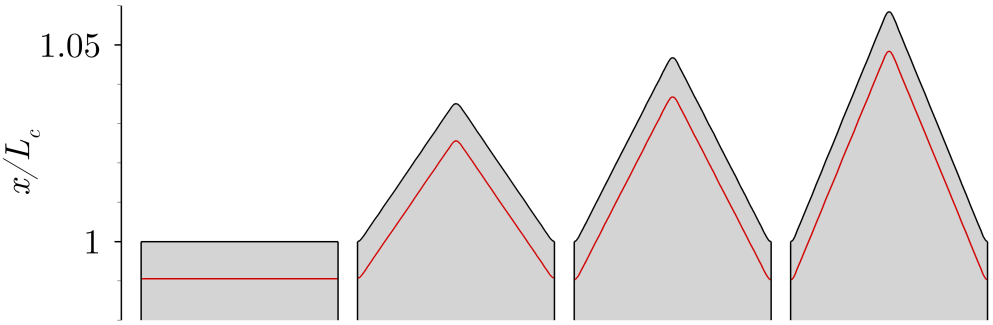

Figure 13: Diagram of the wall pressure fluctuations extraction lines (in red) for all geometries BTE, STE0.75, STE1.00 and STE1.25 from left to right. The diagram is drawn in the JK10 case where the wall pressure fluctuations are taken 1% ahead of the actual trailing edge.

Second, the distribution $S_{qq}(z, \omega)$ is averaged to obtain a representative wall pressure fluctuations spectrum $S_{qq}(\omega)$ which reads

$$S_{qq}(\omega) = \frac{1}{L_s} \int_{-L_s/2}^{L_s/2} S_{qq}(z, \omega) \, \mathrm{d}z, \tag{14}$$

where L_s is the span length. It should be mentioned at this stage that the selection of S_{qq} is critical and highly impacts the result of the model. In principle and following the explanations given by Roger and Moreau [5], the wall pressure fluctuations S_{qq} should be extracted close enough to the TE. They also specify that the chordwise statistics are found to have very little effect on trailing-edge noise. However, existing literature did not study serrated trailing edges and it is not clear at present if the same strategy can be applied. Hence, further investigation is required to clarify this in the future. In reality,

the extraction never occurs exactly on the edge but slightly upstream especially in the case of an LES simulation where the sharp TE is subjected to boundary conditions. After a subsidiary investigation, the authors have found that there exists an optimal location that minimises the relative error with the FW-H results and this location varies between 0.1 and 1% chord upstream of the trailing edge. Thus, the optimal extraction point for the JK10 case was found to lie 1% chord upstream of the trailing edge and the one for the JK12, 0.25% chord upstream of the TE.

Third, a two-dimensional Amiet's noise prediction (derived by Sandberg et al. [50]) is performed at the desired observer location to obtain the far-field sound PSD $S_{pp}(\omega)$. In other words, serrated trailing edges are "reduced" to straight trailing edges with a different representative wall pressure fluctuations spectrum. The assumption is reasonable for calculations far away from the source and the equation reads

$$S_{pp}(\omega) = \left[\frac{\omega L_b(y_o - y_s)}{4\beta a_\infty}\right]^2 |\mathcal{M}|^2 \int \widehat{S}_{qq}(k_1, \omega)\mathrm{d}k_1, \tag{15}$$

where $\widehat{S}_{qq}$ is the wavenumber-frequency PSD of the surface pressure fluctuations and k_1 is the streamwise wavenumber. The integral of $\widehat{S}_{qq}$ can be expressed in terms of the spanwise coherence length and the point-frequency spectrum S_{qq} [51]

$$S_{pp}(\omega) = \frac{1}{\pi}\left[\frac{\omega L_b(y_o - y_s)}{4\beta a_\infty}\right]^2 |\mathcal{M}|^2 S_{qq}(\omega) l_z(\omega), \tag{16}$$

where $L_b = L_c/2$, $\beta = \sqrt{1 - M_\infty^2}$, l_z is the spanwise coherence length and $\mathcal{M}$ reads

$$\mathcal{M} = \int_{x_{LE}}^{x_{TE}} \frac{1}{R_\beta(x,y)} H_D(x,\omega) H_1^{(2)}\{\mu_0[M_\infty(x - x_o) + R_\beta(x,y)]\}\,\mathrm{d}x, \tag{17}$$

$$H_D(x,\omega) = 1 + H_S(x,\omega), \tag{18}$$

$$H_S(x,\omega) = (1 + \boldsymbol{\jmath})E^*\left\{-\left[\mu_0(1 + M_\infty) + \frac{\omega L_b}{u_c}\right]x\right\} - 1, \tag{19}$$

where LE and TE refer to the leading and trailing edges respectively, R_β is defined by

$$R_\beta(x,y) = \sqrt{(x - x_o)^2 + \beta^2(y - y_o)^2}, \tag{20}$$

$H_1^{(2)}$ is the Hankel function of the second kind, E^* is the following combination of Fresnel integrals [4]

$$E^*(s) = \int_0^s \frac{1}{\sqrt{2\pi\xi}} e^{-\boldsymbol{\jmath}\xi}\,\mathrm{d}\xi, \tag{21}$$

$\mu_0 = \omega L_b/(\beta^2 a_\infty)$ and u_c is the convection velocity taken as 70% of the free-stream velocity following a common practice in noise prediction [32, 34]. The simplest and most common model for the spanwise coherence length is Corcos' model [52]. The assumptions of the model are extensively explained by Roger and Moreau [5] and the final formulation reads

$$l_z(\omega) = \frac{b_c u_c}{\omega}, \tag{22}$$

where b_c is an empirical constant. A value of $b_c = 1$ is selected in the present study.

3.2. Application of Amiet's model to serrated trailing edges

The outcome of the model detailed above is presented in this section by focusing on a single observer placed 100 chords away from the TE at $\theta = 90°$ i.e. perpendicular and above the baseline trailing edge. Fig. 14 gathers the PSD functions of the far-field pressure fluctuations for all STE geometries in the JK10 case and compares the results obtained by FW-H calculation and the ones provided by Amiet's model. In practice and to remove the spurious spikes at high frequencies, the raw spectra are extracted over a narrow circular arc between $\theta = 80°$ and $\theta = 100°$ before being line-averaged over the arc. The reader will probably notice that some peaks are present in the FW-H signal. This is investigated

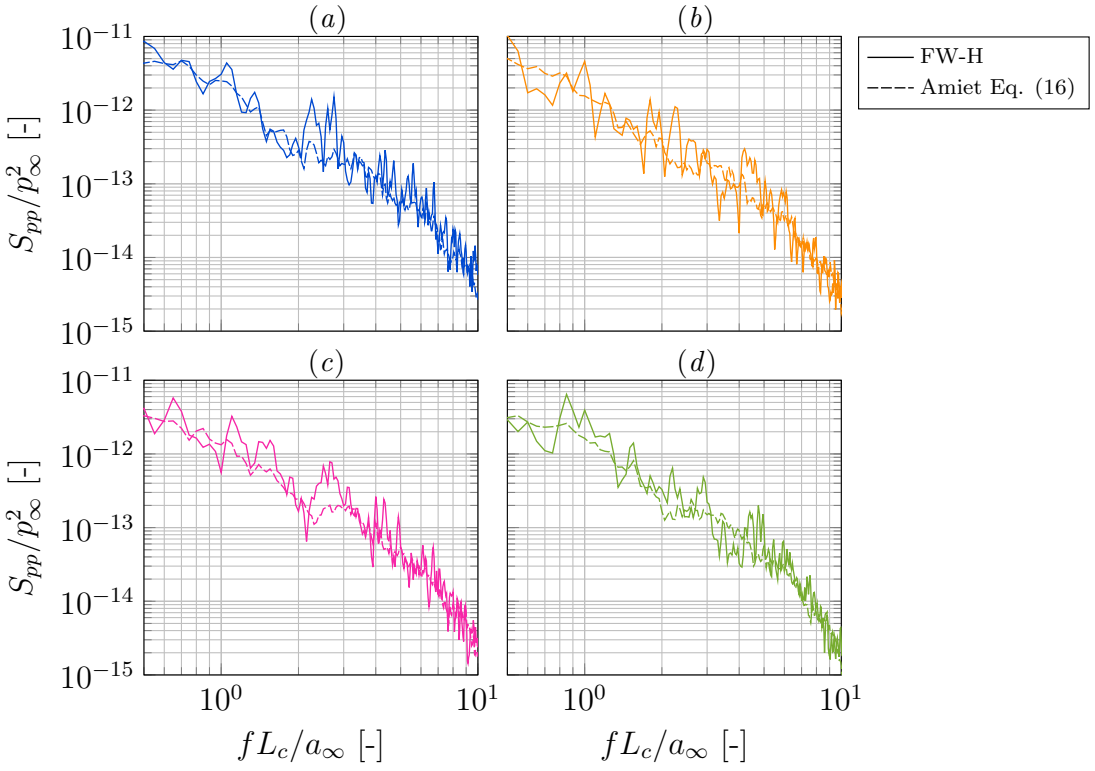

Figure 14: Power spectral density of pressure fluctuations over a narrow circular arc $80° \leq \theta \leq 100°$ of a radius of $R/L_c = 100$ centred at $(x, y, z)/L_c$=(1,0,0) in the JK10 case. The cases displayed are (a) JK10-BTE; (b) JK10-STE0.75; (c) JK10-STE1.00 and (d) JK10-STE1.25.

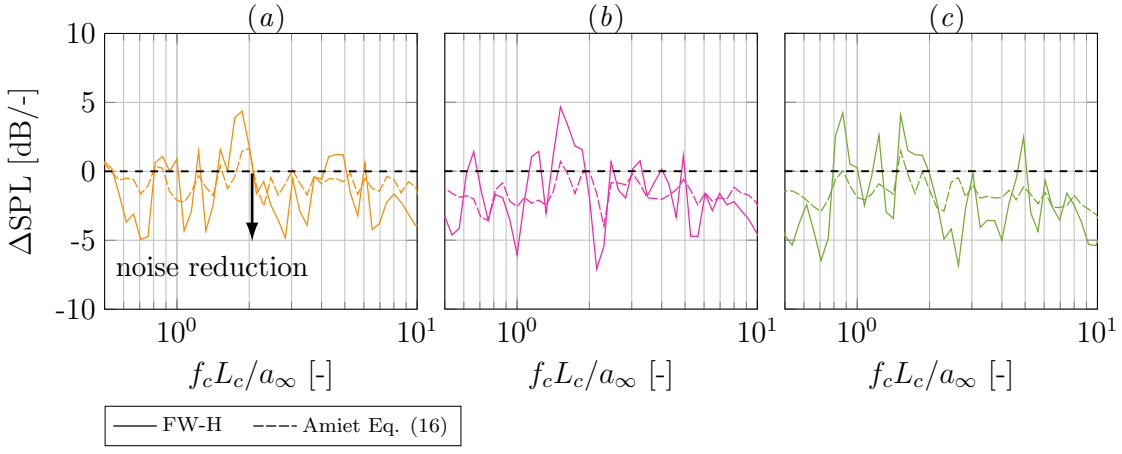

Figure 15: One-tenth octave ΔSPL of (a) JK10-STE0.75, (b) JK10-STE1.00 and (c) JK10-STE1.25 relative to JK10-BTE over a circular arc $80° \leq \theta \leq 100°$ with radius $R/L_c = 100$ centred at $(x, y, z)/L_c$=(1,0,0).

in Appendix B where the authors suggest that these peaks presumably come from the transitional region. However, their presence does not modify the broadband character of the signal. As seen on the plots, both methods are in solid agreement for all trailing-edge geometries. This result is counter-intuitive since Amiet's theory was primarily developed based on a flat-plate aerofoil with a straight trailing edge.

Fig. 15 shows the noise reduction produced by the serrated trailing edges. The observed trend is different from the one found by Avallone et al. [29]. While investigating a thicker NACA0018 aerofoil at $\alpha = 0°$, $M_\infty = 0.06$ and $Re_\infty = 280,000$ with a tripped boundary layer, they observed a peak noise reduction at $fL_c/u_\infty = 8$. No such peak is detected in the present cases. This is perhaps due to very different flow conditions. This statement is supported by the fact that Gruber et al. [53] obtained a relatively flat noise reduction trend as well with closer flow conditions (cambered aerofoil, non zero incidence and higher Mach number) to the current paper.

As shown in Fig. 15, Amiet's model provides a satisfying approximation of the actual noise reduction calculated by the FW-H integration. Some oscillations are still present in both the PSDs and SPL differences since the results will not perfectly collapse but the mean trend of the noise reduction over the frequency range of study is well-captured by Amiet's theory according to the present results. The next section aims to bring an explanation for the current observations.

4. Why does Amiet's model work for serrated trailing edges?

This section depicts a detailed spectral analysis of the wall pressure fluctuations (noise source) near TE to explain why Amiet's theory works remarkably well for serrated trailing edges although it was not originally derived for them. First, the distribution of noise sources is examined. Second, an FW-H calculation is performed by removing the phase shift between all aerofoil surface points located in the vicinity of the TE. The following study focuses on the JK10 aerofoil cases for which all STE geometries are available.

4.1. Distribution of the noise sources along the TE

Fig. 16 shows the cosine function of the phase ϕ in the Fourier transform of the surface pressure fluctuations i.e. $\cos\phi = \mathrm{Re}(\Delta P_w)/|\Delta P_w|$ where the operator "Re" denotes the real part. Fig. 17 and 18 display the PSD function of the wall pressure fluctuations. Since the object of the study is the noise generated by TE scattering, the near-TE region is solely exhibited. Taking into account the broadband character of the signals, the PSDs are integrated on one-third octave bands to summarize the spectral information. Thus, the resulting PSD plots are displayed at central frequencies $f_c L_c/a_\infty$ which represent the middle of an octave frequency band. If the phase distribution pattern (Fig. 16) on the wall looks very similar across all TE geometries, a different observation can be made from the source magnitude plots (Fig. 17 and 18). In agreement with the investigations performed by Avallone et al. [29], it is clear that the strength of wall pressure fluctuations (WPF) changes significantly (by one order of magnitude) between the root and the tip of the sawtooth serration and the phenomenon becomes increasingly pronounced when a sharper serration is used. In the STE1.00 and STE1.25 cases, a clear weak WPF spot is detected at the tip of the serrations. The authors have observed the same pattern across the entire frequency range as indicated in Fig. 17 and 18. The above suggests that the change in WPF magnitude along the TE may has a significant impact on the radiated sound. A further investigation using FW-H approach is provided below.

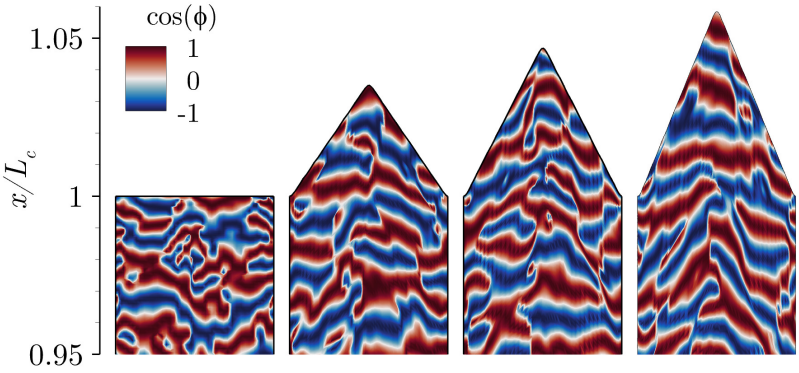

Figure 16: Source phase distribution (based on wall pressure fluctuations) on the suction side of the JK10 aerofoil at $fL_c/a_\infty = 8$ for all trailing edge geometries: BTE, STE0.75, STE1.00, STE1.25 from left to right. Red and blue are out of phase to each other.

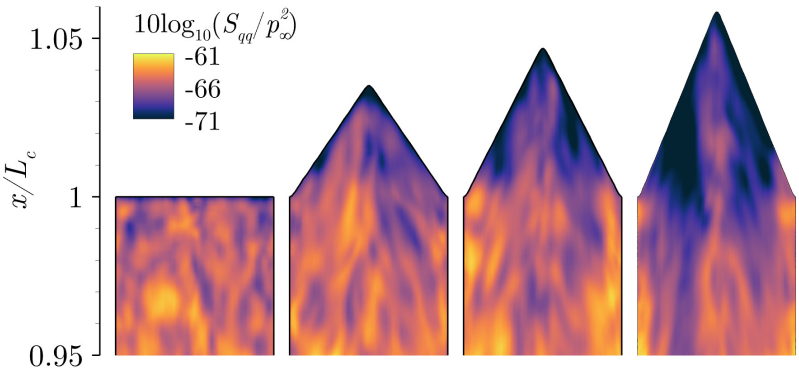

Figure 17: Contour maps of the PSD function of the surface pressure fluctuations in log scale on the suction side of the JK10 aerofoil at $f_cL_c/a_\infty = 8$ for all trailing edge geometries: BTE, STE0.75, STE1.00, STE1.25 from left to right.

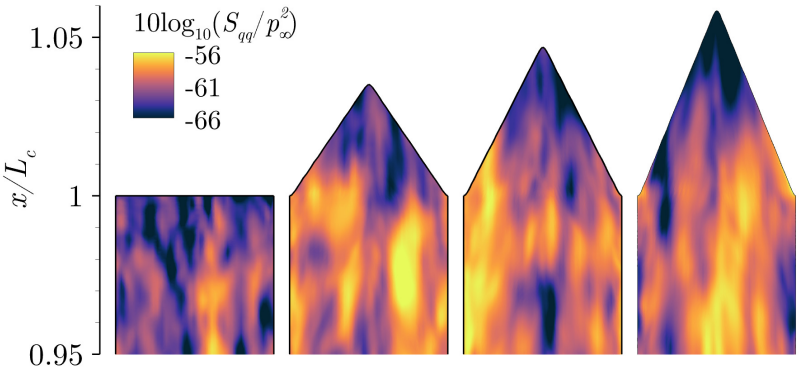

Figure 18: Contour maps of the PSD function of the surface pressure fluctuations in log scale on the suction side of the JK10 aerofoil at $f_cL_c/a_\infty = 1$ for all trailing edge geometries: BTE, STE0.75, STE1.00, STE1.25 from left to right.

4.2. Source phase effects on the far-field sound

To the best of the authors' knowledge, all STE noise prediction methods to date are based on the same hypothesis which stipulates that the phase distribution of wall pressure fluctuations near the TE produce destructive phase interferences in the scattered pressure resulting in noise abatement. To understand why Amiet's theory, which does not

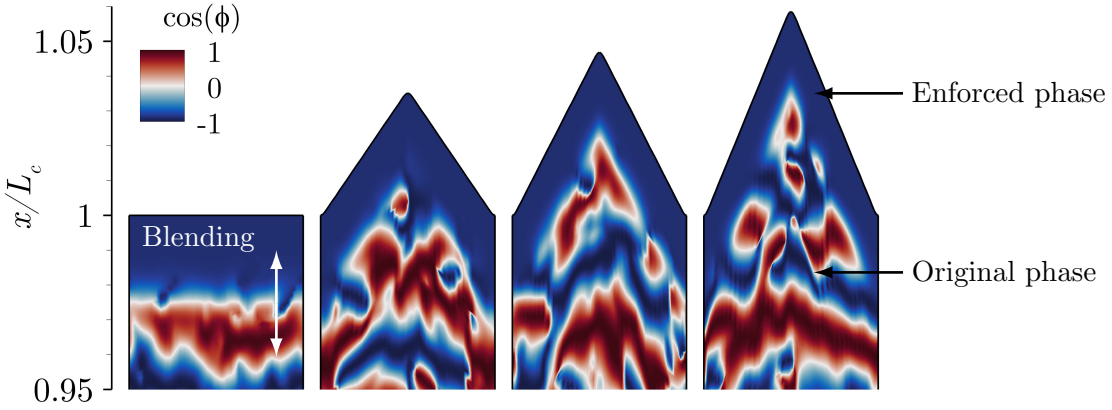

Figure 19: Source phase distribution of the modified wall pressure $\tilde{p}$ on the suction side of the JK10 aerofoil at $fL_c/a_\infty = 4$ for all trailing edge geometries: BTE, STE0.75, STE1.00, STE1.25 from left to right. Red and blue are out of phase to each other.

include such phase information, works for serrated trailing edges as well as the baseline, an attempt has been made to remove the phase variation of the source near the TE to investigate their effect on the radiated sound using FW-H approach. The current FW-H calculation is performed by using Eq. (4) and (5) on the aerofoil surface. The LES surface mesh and solution are directly used for the FW-H calculation. Then, an additional FW-H calculation is carried out by using modified surface pressure data (time signals). The signal modification is intended to remove the phase variation in the source near the TE so that all phase interference effects are manually turned off while preserving the average phase information for each frequency. This is achieved in the following way

$$\widetilde{p}(\boldsymbol{x},t) = w(\boldsymbol{x})\mathcal{F}^{-1}\Big\{\big|\mathcal{F}[p(\boldsymbol{x},t)]\big|(\cos\phi_0 + \boldsymbol{j}\sin\phi_0)\Big\} + [1-w(\boldsymbol{x})]p(\boldsymbol{x},t), \tag{23}$$

where $\widetilde{p}$ is the modified pressure, $\mathcal{F}$ and $\mathcal{F}^{-1}$ represent the Fourier and inverse Fourier transforms respectively, ϕ_0 is the surface-averaged phase enforced in the near-TE region

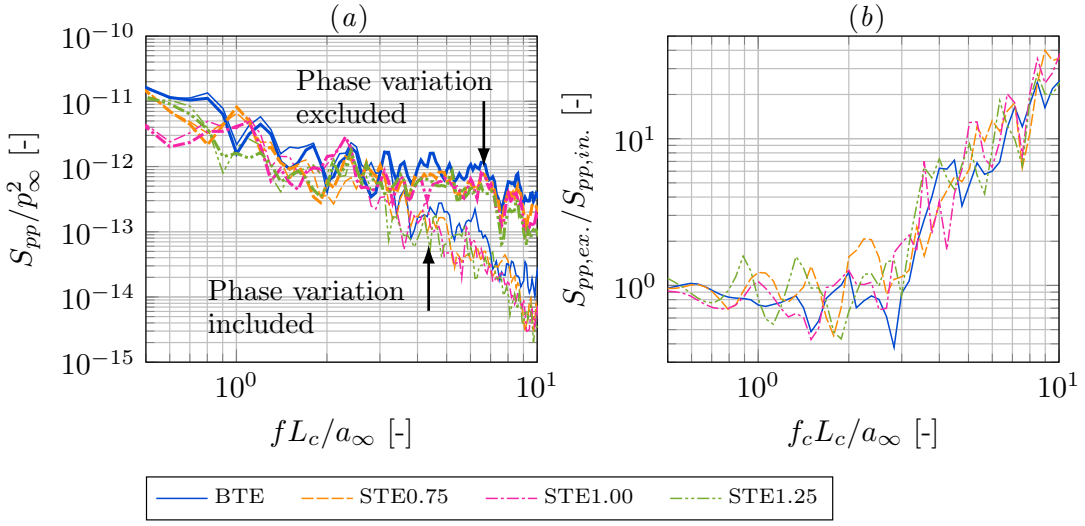

Figure 20: (a) PSD over a narrow circular arc $80^\circ \leq \theta \leq 100^\circ$ of a radius of $R/L_c = 100$ centred at the TE of the BTE case $(x, y, z)/L_c$=(1,0,0). The thinner lines are obtained with the source phase variation included and the thicker ones with the source phase variation excluded. (b) Corresponding PSD ratio of the results obtained by excluding ($S_{pp,ex.}$) and including ($S_{pp,in.}$) the source phase variation.

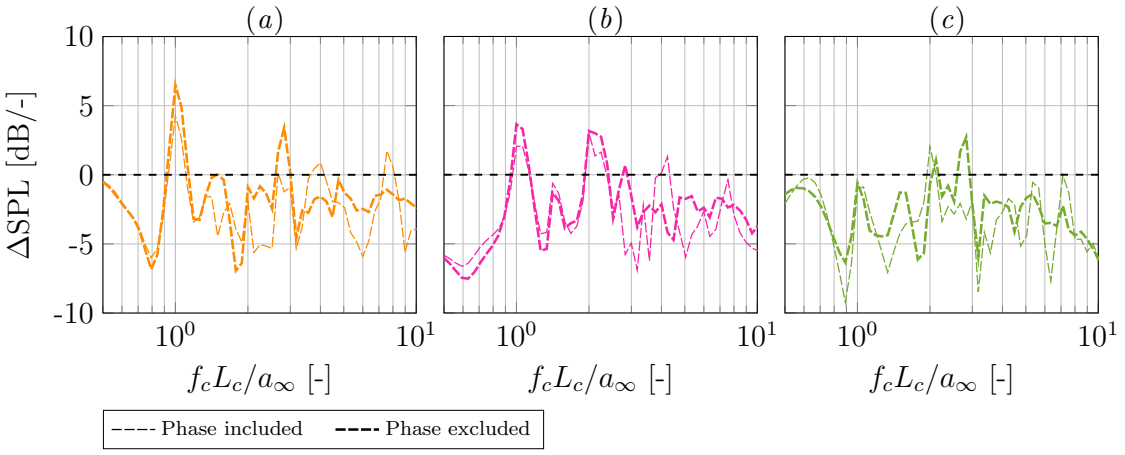

Figure 21: One-twelfth octave ΔSPL of (*a*) JK10-STE0.75, (*b*) JK10-STE1.00 and (*c*) JK10-STE1.25 relative to JK10-BTE over a narrow circular arc $80^\circ \leq \theta \leq 100^\circ$ of a radius of $R/L_c = 100$ centred at the TE of the BTE case $(x, y, z)/L_c$=(1,0,0). The thinner lines are obtained with the source phase variation included and the thicker ones with the source phase variation excluded.

and $w(\boldsymbol{x})$ is a blending function which ensures a smooth transition between the original and enforced phase. To better illustrate the process, a new source phase contour map is displayed in Fig. 19 where the phase variation removal near the TE is depicted. The current settings are such that the smooth blending occurs across 3% of the chord and that the source phase variations are completely removed over the last 1% of the chord. The results are shown in Fig. 20*a*. The thinner lines show the FW-H spectra obtained with the real WPF source and the thicker lines show the results collected with the modified source.

The first observation, supported by Fig. 20*b*, is that the elimination of the phase variation gives rise to the far-field SPL by up to 15 dB in the high-frequency range. This indicates the significance of (destructive) phase interference effects on the radiated sound. The second observation is that, despite the change due to the removed phase variation, the ratio between the quantities obtained by excluding and including the phase variation (Fig. 20*b*) is consistent throughout the frequency range and for all TE geometries. This remark is further supported by Fig. 21 where the STE noise reduction is plotted on a decibel scale. The noise reduction (or increase) due to the STEs relative to the BTE case seems consistent across a wide range of frequencies regardless of whether the source phase variation is included or excluded. This suggests that noise reduction due to STEs may be reasonably well predicted by using the source magnitude data with no phase variation information.

In order to check the validity of the above observation, wall-pressure coherence in the vicinity of the TE is examined in Fig. 22. The plots are obtained by using Eq. (10) along the path-lines displayed in Fig. 13. The reference point $\boldsymbol{x}_1$ is taken at $z = -L_s/2$ corresponding to the root of the STEs and the points $\boldsymbol{x}_2$ cover half of the span. The spanwise displacement between $\boldsymbol{x}_2$ and $\boldsymbol{x}_1$ is denoted by Δz. Fig. 22 explores three different central frequencies and shows that the level of coherence along the TE path-line is comparable between the BTE and STE cases. In other words, the STE cases do not exhibit a significant reduction in coherence compared to the BTE case, which is in line with the earlier observation from the FW-H data. Fig. 23 shows the spanwise coherence length as a function of frequency obtained from the following definition [5]

$$l_z(f) = \int_0^\infty \sqrt{\gamma_c^2(\Delta z, f)}\, \mathrm{d}\Delta z, \tag{24}$$

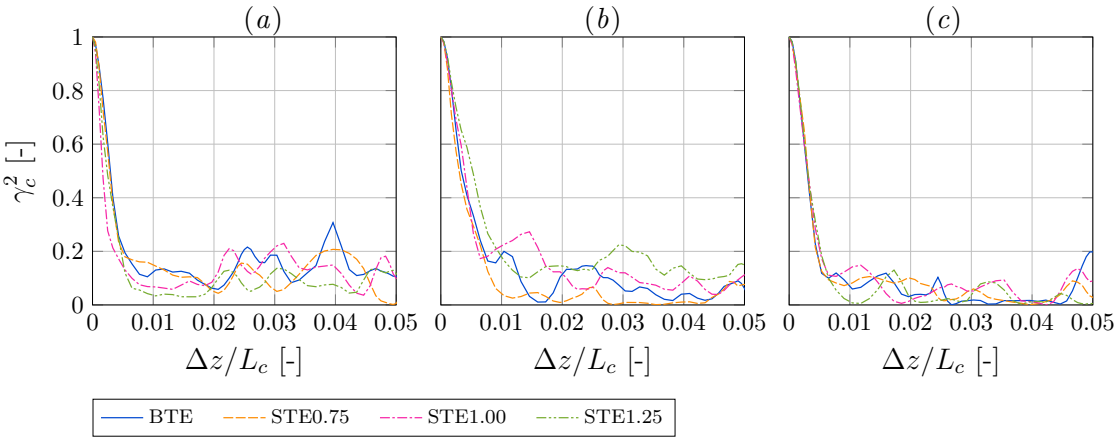

Figure 22: One-fifth octave coherence along a path-line near the TE (Fig. 13) at central frequencies (a) $f_c L_c/a_\infty = 0.5$; (b) $f_c L_c/a_\infty = 2$ and (c) $f_c L_c/a_\infty = 8$. The reference point is located at $z = -L_s/2$ and Δz designates the spanwise displacement in the two-point cross-correlation.

where $\gamma_c^2(\Delta z, f)$ is the two-point coherence and Δz is the spanwise displacement between those points. Although the calculation is not entirely reliable due to the inherent limitations of LES simulations (i.e. limited span and periodic boundary condition), the results still agree with the above observation - there are insignificant discrepancies between the BTE and STE cases in terms of the spanwise coherence length. Furthermore, the level of l_z is comparable to the semi-empirical prediction of Corcos' model as shown in the figure.

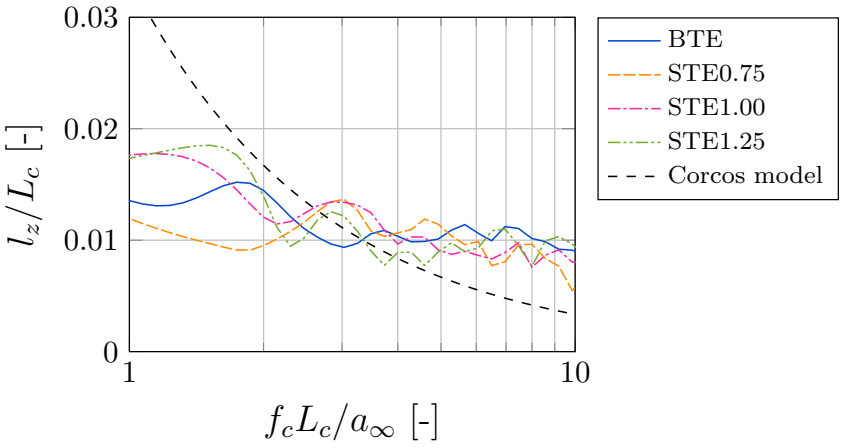

Figure 23: Spanwise coherence length from Eq. (24) at the reference point located at $z/L_c = -L_s/2$.

In summary, the study in this section suggests that the reduced WPF magnitude is the primary mechanism of noise reduction offered by STEs. On the other hand, no significant change in the spanwise coherence (phase interference) is found between the BTE and STE cases. This justifies the use of Amiet's theory for STEs with no special treatment on the spanwise coherence length (l_z). However, one caveat is that Amiet's model requires a path-line averaged WPF spectrum (S_{qq}) which is not achievable without a 3-D simulation or measurement. There is a scope of future work to develop a semi-empirical model for this.

5. Proposition of directivity correction

In section 3.2, Amiet's model proved to perform strongly for an observer located right above the TE at $\theta = 90°$. However, in the upstream and downstream directions, the model can capture the PSD slope but fails to accurately predict the magnitude as shown in Fig. 24 which depicts the far-field PSD obtained via FW-H and Amiet's model in the JK10-BTE case. This observation is confirmed by Fig. 25 where the directivity patterns of the PSD are displayed at four different frequencies. The existence of such a difference between FW-H and Amiet results is perhaps attributed to the assumptions of the latter. FW-H is based on a mathematical integration of the entire aerofoil surface pressure fluctuations and thus, delivers a real noise prediction by taking into account the aerofoil shape and thickness as well as the flow direction whereas Amiet's model is based on a flat-plate formulation without any angle of attack.

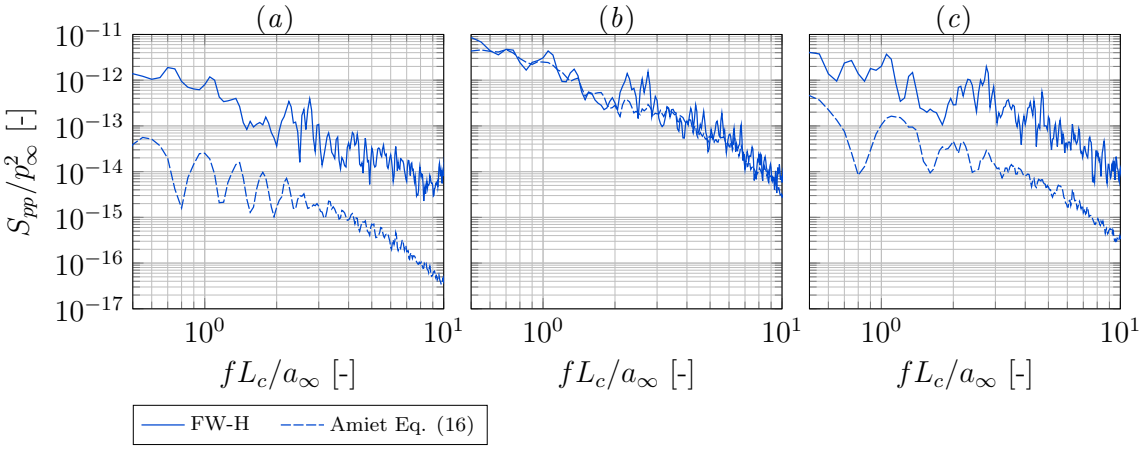

Figure 24: Power spectral density of pressure fluctuations at 100 chords away from the TE in the JK10-BTE case for observer angles (a) $\theta = 30°$; (b) $\theta = 90°$ and (c) $\theta = 150°$.

The gap existing between Amiet's and FW-H results has motivated the elaboration of a directivity correction factor $D(\theta)$. The correction principle is rather simple and consists of modifying Amiet's formula in the following fashion

$$S_{pp}(\omega) = \frac{D(\theta)}{\pi}\left[\frac{\omega L_b(y_o - y_s)}{4\beta a_\infty}\right]^2 |\mathcal{M}|^2 S_{qq}(\omega) l_z(\omega). \tag{25}$$

The estimation of this gap comes from the study of the ratio of FW-H and Amiet's PSDs which are calculated for all cases and all angles. The ratios are integral-averaged over the desired frequency range and averaged over all cases. The overall result of the process is a global objective ratio $D_{obj}(\theta)$ which reads

$$D_{obj}(\theta) = \frac{1}{N_c}\sum_{n=1}^{N_c}\frac{1}{f_b - f_a}\int_{f_a}^{f_b}\frac{S^F_{pp,n}(f,\theta)}{S^A_{pp,n}(f,\theta)}\,\mathrm{d}f, \tag{26}$$

where $[f_a, f_b]$ is the frequency interval of integration, $N_c = 11$ is the total number of cases, $S^F_{pp,n}$ and $S^A_{pp,n}$ are the PSDs from FW-H and Amiet's original model respectively and n is the index referring to the case reference number in Table 1. The objective function $D_{obj}(\theta)$ is plotted in Fig. 26 for $[f_a, f_b] = [0.5, 10]$. Multiple strategies have been explored by the authors for the construction of a mathematical function that would best approach

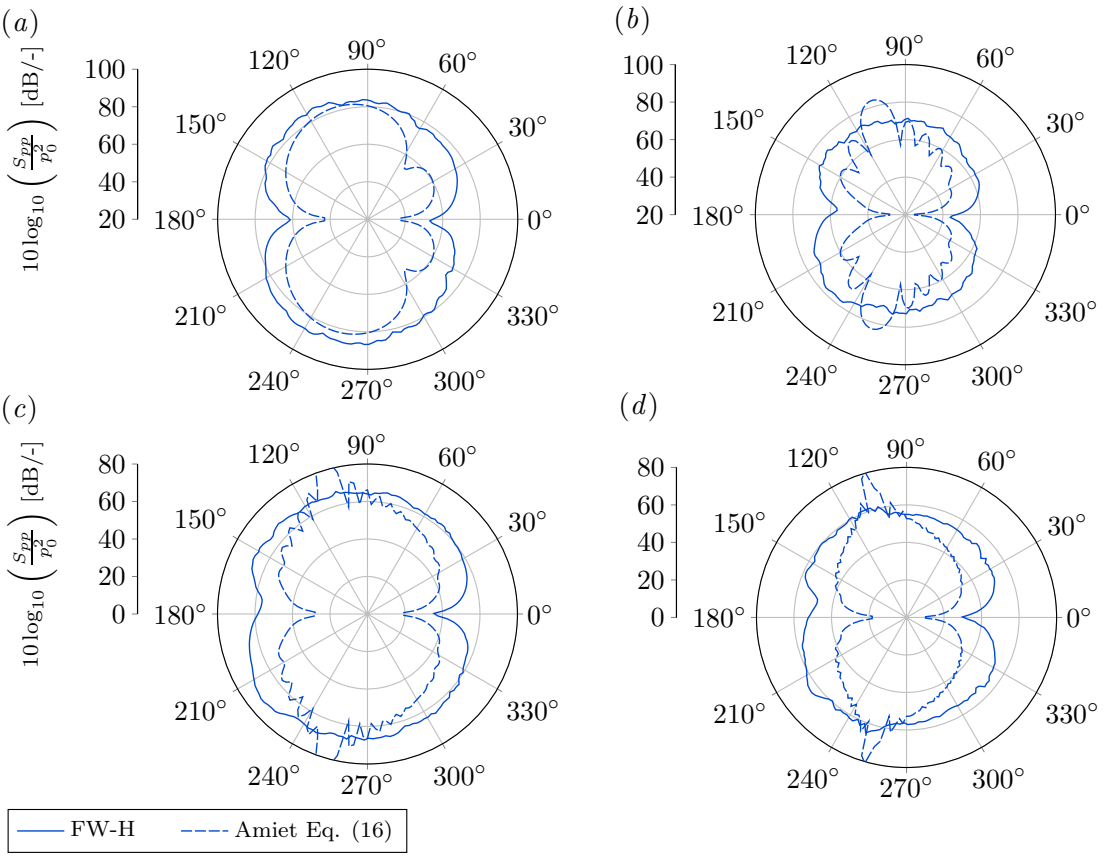

Figure 25: Directivity pattern of the one-fifth octave-integrated PSD of pressure fluctuations at 100 chords away from the TE in the JK10-BTE case at central frequencies (a) $f_c L_c/a_\infty = 0.5$; (b) $f_c L_c/a_\infty = 2.0$; (c) $f_c L_c/a_\infty = 4.0$ and (d) $f_c L_c/a_\infty = 8.0$.

a_0	a_1	a_2	a_3	a_4	a_5
50.01470	-5.11966	62.00000	-13.78140	12.98500	-6.09897

Table 2: Values of the optimised coefficients a_n of the directivity correction function $D(\theta)$.

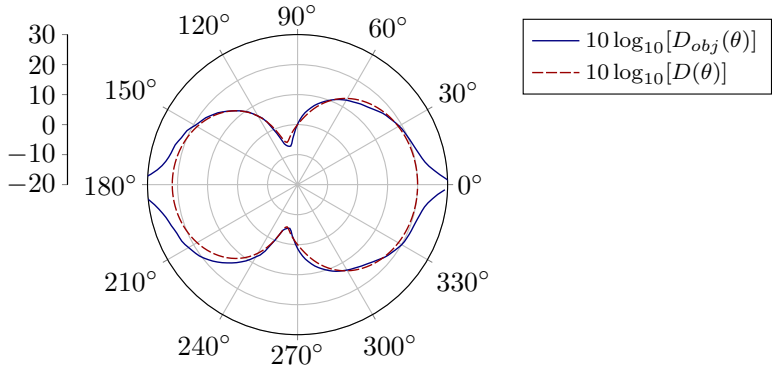

Figure 26: Graphical representation in log scale and in polar coordinates of the objective function $D_{obj}(\theta)$ and the directivity correction factor $D(\theta)$ using the coefficients in Table 2.

$D_{obj}(\theta)$ since the polar shape to model is very complex. The most satisfactory and elegant

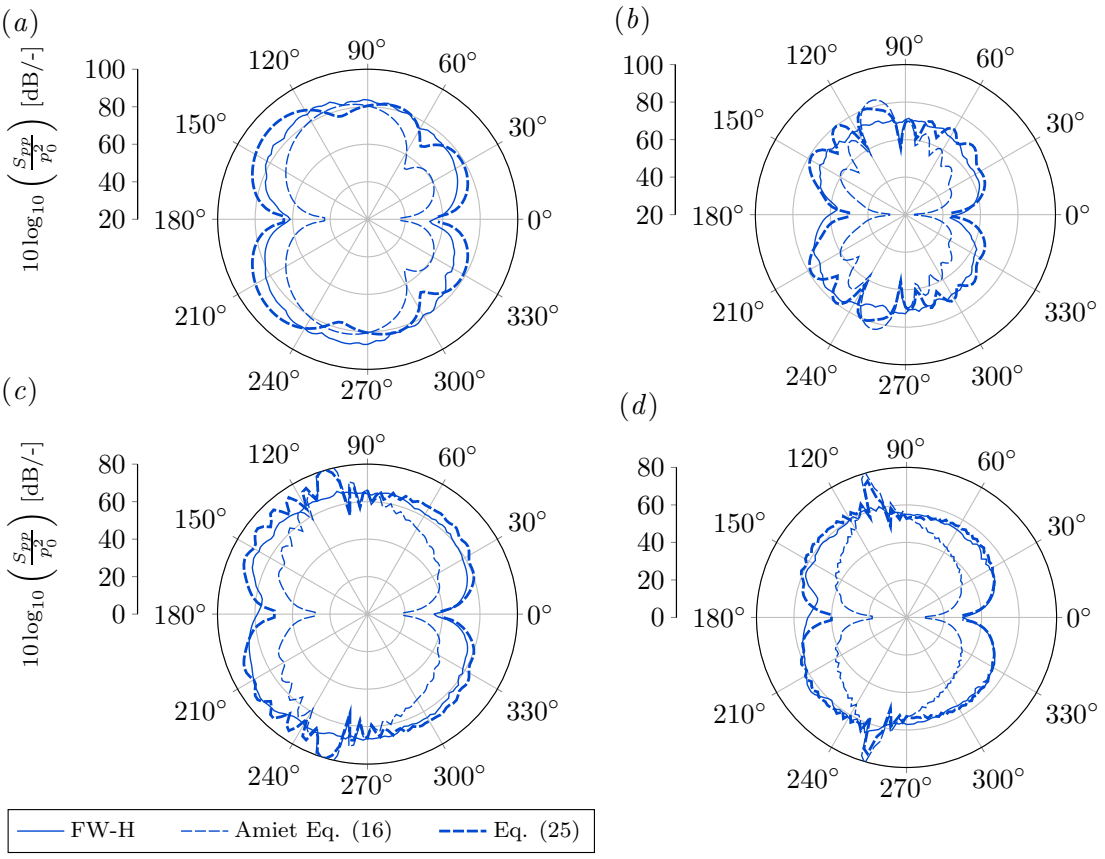

Figure 27: Directivity pattern of the one-fifth octave-integrated PSD of pressure fluctuations at 100 chords away from the TE in the JK10-BTE case at central frequencies (*a*) $f_c L_c/a_\infty = 0.5$; (*b*) $f_c L_c/a_\infty = 2.0$; (*c*) $f_c L_c/a_\infty = 4.0$ and (*d*) $f_c L_c/a_\infty = 8.0$.

formulation was provided by a finite series of cosine functions which reads

$$D(\theta) = \sum_{n=0}^{5} a_n \cos(n\theta), \tag{27}$$

where $\theta \in [0°, 360°]$ is the directivity angle with origin the x-axis i.e. $\tan\theta = (y_o - y_s)/(x_o - x_s)$. The coefficients a_n are determined following a few conditions. The most important one is that the magnitude of the far-field sound provided by Amiet's original model should remain the same at $\theta = 90°$ since the prediction is already accurate at this particular angle. The values in Table 2 are optimised for the JK10 and JK12 cases including all TE geometries. A graphical representation of $D(\theta)$ is also provided in Fig. 26. The directivity correction function is symmetric with respect to the x-axis and a value $D(\theta) = 1$ is preserved at $\theta = 90°$ and $\theta = 270°$. The agreement between $D(\theta)$ and the objective function $D_{obj}(\theta)$ is satisfactory for a wide range of angles $\theta \in [30°, 150°] \cup [210°, 330°]$.

As shown in Fig. 27 and 28, the application of the directivity correction in the JK10-BTE and JK12-BTE cases improves the prediction of the sound in all directions independently of the frequency, keeping the correction as simple as possible. The magnitude which fails to be correctly captured by Amiet's model alone at $\theta = 30°$ and $\theta = 150°$ is a lot more satisfactory with respect to FW-H results after the introduction of the correction factor $D(\theta)$. At high frequencies and for the angular region lying between $\theta = 100°$ and $\theta = 110°$, the original prediction method shows a noise over-prediction which the directivity correction helps to mitigate. The sound in the regions close to $\theta = 0°$ or $\theta = 180°$ corresponding to the direct downstream and upstream directions remains slightly under-predicted. The

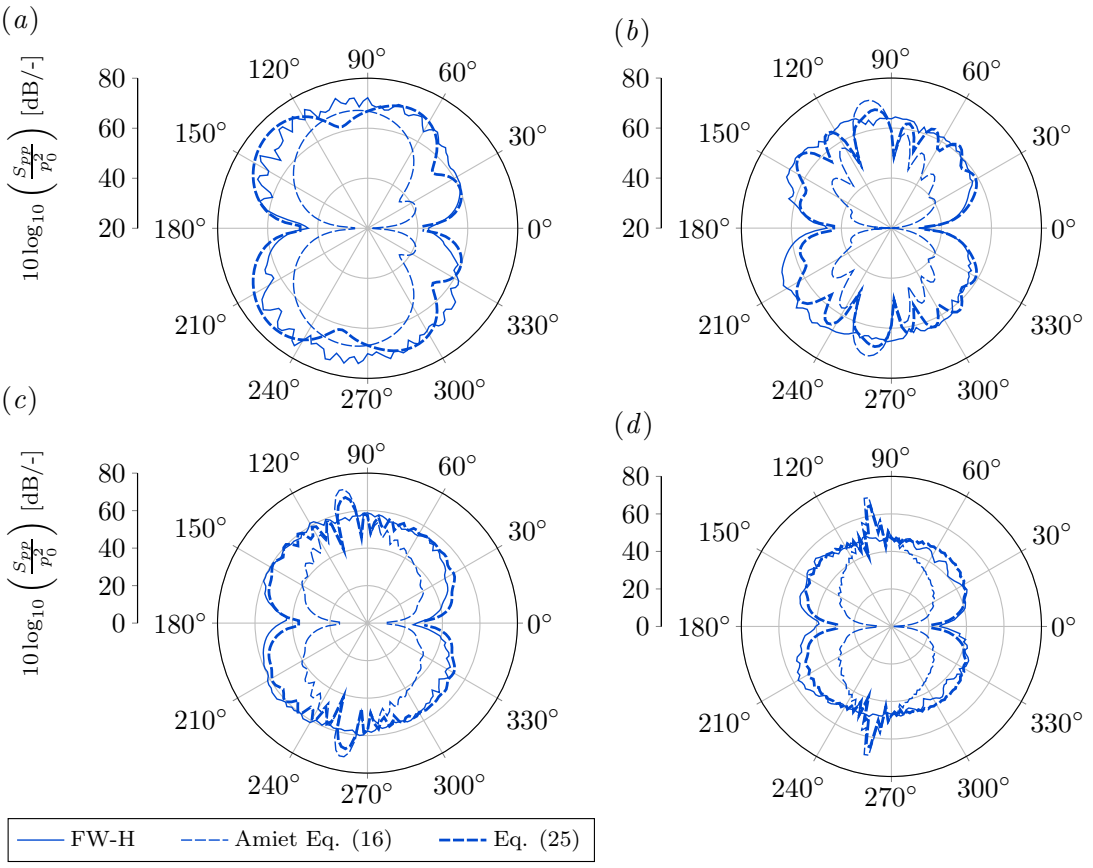

Figure 28: Directivity pattern of the one-fifth octave-integrated PSD of pressure fluctuations at 100 chords away from the TE in the JK12-BTE case at central frequencies (*a*) $f_c L_c/a_\infty = 0.5$; (*b*) $f_c L_c/a_\infty = 2.0$; (*c*) $f_c L_c/a_\infty = 4.0$ and (*d*) $f_c L_c/a_\infty = 8.0$.

only limitation of the correction factor comes from the inclusion of all cases. Since JK10 and JK12 cases present some slight changes in PSD magnitude depending on the frequency and angle, the optimisation finds a trade-off. In the upstream direction, this results in noise over-prediction in the JK10 case and noise under-prediction in the JK12 case. Nevertheless, the directivity correction provides a much more satisfactory noise prediction overall. The amelioration of the model applies for BTE but also for the different STEs as illustrated in Fig. 29. This figure shows that the directivity correction factor contributes to recover a closer OASPL to FW-H for most of the directivity angles and all STEs.

6. Predicting the noise reduction with the new proposed model

The present section focuses on the noise-reduction prediction using Amiet's model. The noise reduction is studied in details by plotting the relative difference between each STE case and the BTE case. Fig. 30 gathers the SPL relative difference for three different angles and all STE cases in the JK10 case. The results obtained using Eq. (25) are solely displayed since the directivity correction does not impact the relative difference between spectra. Although the noise prediction from Amiet's model is not as oscillatory as FW-H, the overall shape of ΔSPL is well-captured. The agreement between FW-H and Amiet's model also stands for the OASPL relative difference as shown in Fig. 31. ΔOASPL slightly varies depending on the directivity angle in the FW-H case whereas the prediction provided by Amiet's model is flatter over the angle range. However, the model manages to successfully capture the magnitude for all angles.

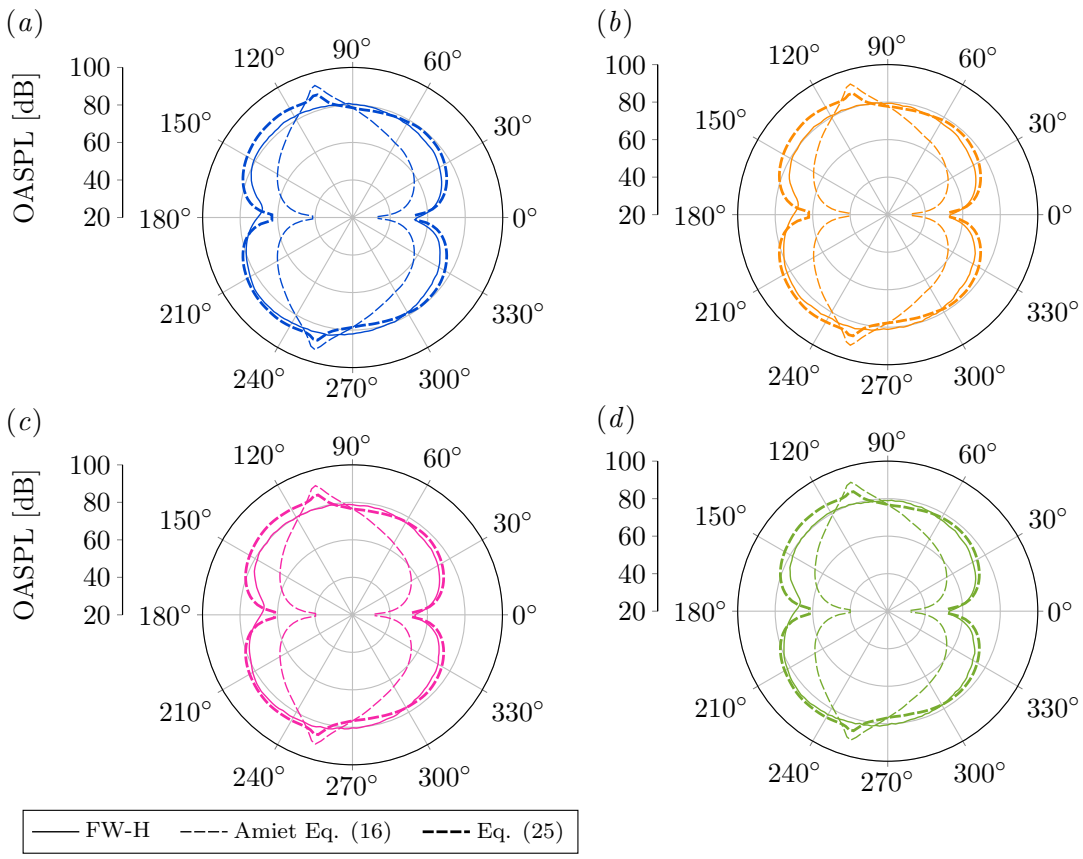

Figure 29: Directivity pattern of the OASPL at 100 chords awaw from the TE in the JK10 case for (a) BTE; (b) STE0.75; (c) STE1.00 and (d) STE1.25.

The observations made in the JK10 case are further supported by Fig. 32 and 33 which respectively display the ΔSPL and ΔOASPL in the JK12 case. The results obtained using Lyu & Ayton's [34] model are also added to these figures to compare the performances in terms of noise-reduction prediction. The aforementioned model uses the spanwise-averaged BTE wall pressure fluctuations extracted at the same location as for Amiet's predictions (0.25% ahead of the TE in the JK12 case). The BTE prediction is obtained by setting the serration length to zero in the model. The SPL difference is again really well-captured by Amiet's model compared to FW-H results whereas Lyu & Ayton's model tends to over-predict the noise reduction at almost all frequencies in the investigated directions. The ΔOASPL deviation between the model and FW-H is increased in the present case compared to the JK10 case but remains comprised within 1 or 2 dB. In terms of ΔOASPL, Lyu & Ayton's model presents the advantage of having the same slope as FW-H from downstream to upstream angles however, the magnitude is consistently under-predicted by around 5 dB.

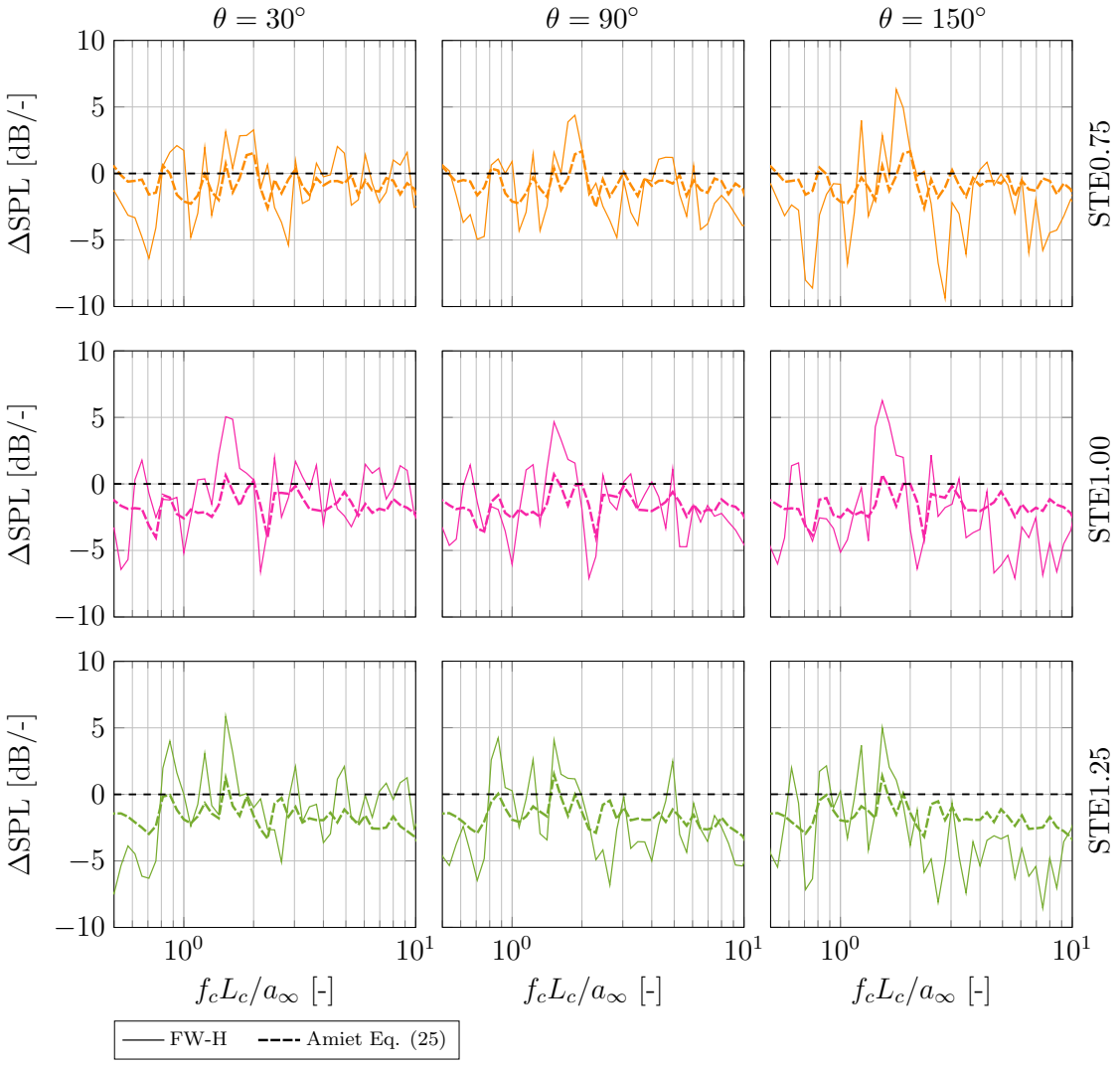

Figure 30: Relative SPL difference of pressure fluctuations over one-tenth octave bands. Calculations are made over a narrow circular arc centred on θ of width 12° and a radius of 100 chords centred at the TE in the JK10 case. The figure gathers plots for three different directions (left to right) and for each STE geometry (top to bottom).

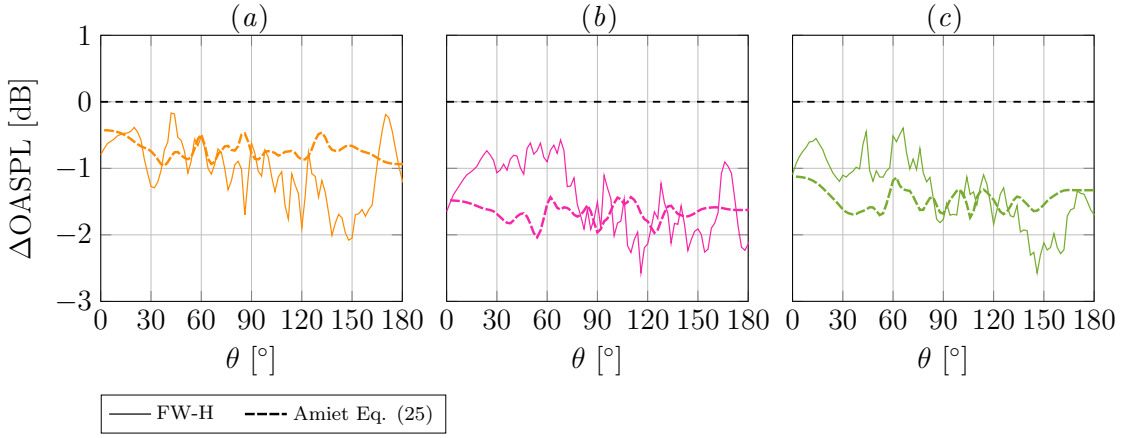

Figure 31: Relative difference of OASPL at 100 chords away in the upper semi-circle above the TE in the JK10 case for (a) STE0.75; (b) STE1.00 and (c) STE1.25.

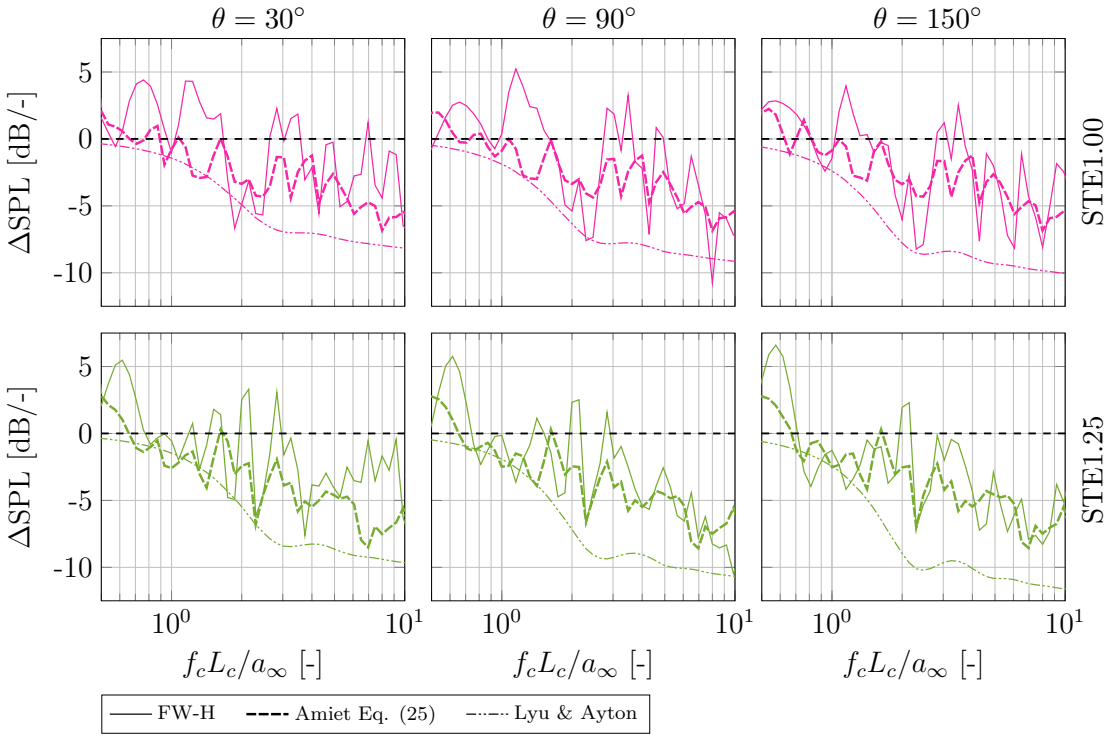

Figure 32: Relative SPL difference of pressure fluctuations over one-tenth octave bands. Calculations are made over a narrow circular arc centred on θ of width 12° and a radius of 100 chords centred at the TE in the JK12 case. The figure gathers plots for three different directions (left to right) and for each STE geometry (top to bottom). Lyu & Ayton's results are computed based on their rapid model [34].

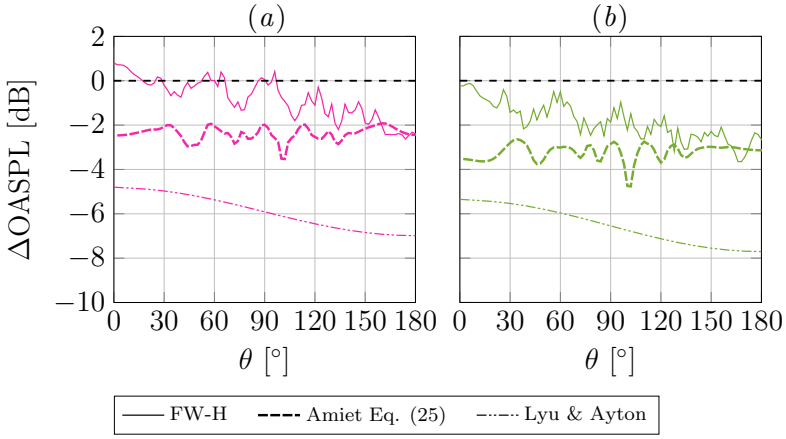

Figure 33: Relative difference of OASPL at 100 chords away in the upper semi-circle above the TE in the JK12 case for (a) STE1.00 and (b) STE1.25. Lyu & Ayton's results are computed based on their rapid model [34].

7. Conclusions

High-fidelity numerical simulations have been carried out using Joukowski aerofoils (10% and 12% thickness) in two different flow conditions $Re_\infty = 300\ 000$; $M_\infty = 0.3$; $\alpha = 6.5°$ and $Re_\infty = 500\ 000$; $M_\infty = 0.2$; $\alpha = 6.0°$ in order to show the feasibility of using Amiet's model for the prediction of broadband noise generated from serrated trailing edges.

As the first main outcome of the present study, the authors showed that Amiet's model accurately predicted the sound pressure level generated from serrated trailing edges. The model proved to perform very well in the 90 and 270 degrees of observer angles from the

TE. Consequently, at these angles, the noise reduction due to the serrated trailing edges was accurately predicted within a tolerance of 1 or 2 dB. The results in section 4 suggested that the source magnitude decreased when an STE was used, which was the main driver of the noise reduction. In contrast, the source phase effect that governs the spanwise coherence length remained fairly constant for both BTE and STE cases and therefore did not make a significant contribution to the noise reduction. This investigation provided a plausible explanation as to how Amiet's model successfully predicted the STE noise without modifying the spanwise coherence length $l_z(\omega)$.

Amiet's original model that was derived from a zero-thickness flat plate failed to correctly capture the noise level from a thicker Joukowski aerofoil in the observer angles other than 90 and 270 degrees. This under-prediction is also well documented in the previous literature. In order to address this issue, the authors proposed a directivity correction factor as a function of the observer angle, obtained from combining 11 different high-fidelity LES cases conducted for this work. It is worth noting that the directivity correction was insensitive to the frequency and the TE geometry as far as the current cases were concerned. The directivity correction resulted in a more accurate and reliable sound prediction in all observer angles for both serrated and baseline trailing edges. The modified Amiet's model offered an accurate prediction of the reduced noise due to STEs within a 1 or 2 dB deviation in terms of OASPL from the corresponding FW-H prediction, at all observer angles. However, it remains to be seen if the modified Amiet's model will work consistently well for other types of aerofoils in significantly different loading conditions. There is a scope of further study on this.

For practical applications of the modified Amiet's model for STE, a fast semi-empirical calculation of the TE line-averaged wall pressure spectrum is required as the source input. Currently, very little is known about the STE wall pressure spectra in order to achieve such a semi-empirical model. There is an urgent need to carry out investigations on this particularly from industrial perspectives.

Acknowledgement

The authors would like to thank VESTAS for this project with special acknowledgement to Mr Diogo Samora Cerqueira and Mr Tomas Vronsky. We also acknowledge EPSRC (Engineering and Physical Sciences Research Council) for the UK supercomputing facility ARCHER made available for this work via UK Turbulence Consortium (EP/R029326/1). Besides, we would like to acknowledge the high-performance computing facility IRIDIS 5 and associated support services at the University of Southampton in the completion of this research. All data supporting this study are openly available from the University of Southampton repository at http://dx.doi.org/10.5258/SOTON/XXXXXX.

Appendix A. Impact of the span length and length of extracted time signal

A brief span length study is reported in this section. On top of the four cases JK10-BTE, JK10-STE0.75, JK10-STE1.00 and JK10-STE1.25 which all use a span of 5% chord and resolve one serration between the spanwise boundaries, JK10-BTE-ext., JK10-STE0.75-ext., JK10-STE1.00-ext. and JK10-STE1.25-ext. cases have been simulated using a span extended to 10% chord. These cases resolve two serrations.

Fig. A.34 displays the far-field PSDs in the BTE and STE1.25 cases by comparing the span lengths. Although the overall order of magnitude of the PSDs remains similar, a slight difference is noticeable at lower frequencies (Fig. A.34*b*). This is reasonably attributed to the fact that the larger span case is able to resolve larger spanwise turbulent

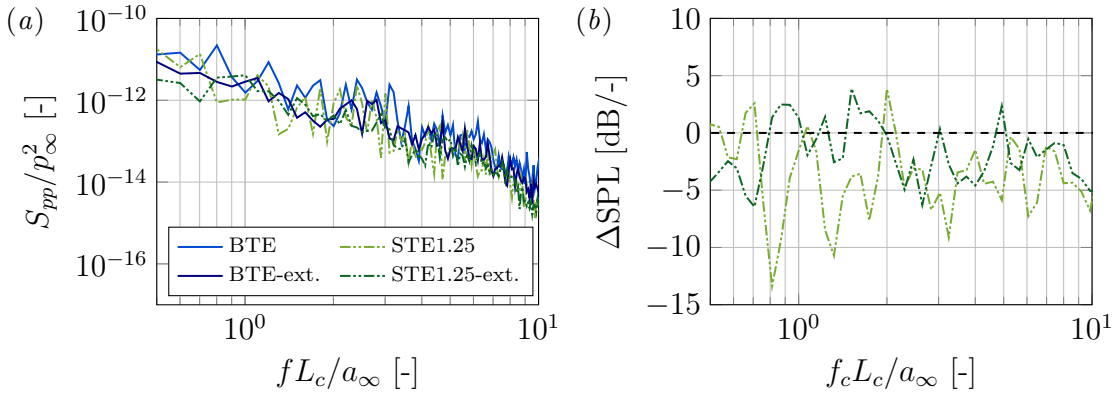

Figure A.34: Comparison of two span lengths in terms of the PSD of pressure fluctuations over a narrow circular arc $80^\circ \leq \theta \leq 100^\circ$ of a radius of $R/L_c = 100$ centred at the TE of the BTE case $(x, y, z)/L_c$=(1,0,0): (a) the individual PSDs and (b) the relative difference of the STE1.25 case to the baseline in decibels over one-tenth octave bands.

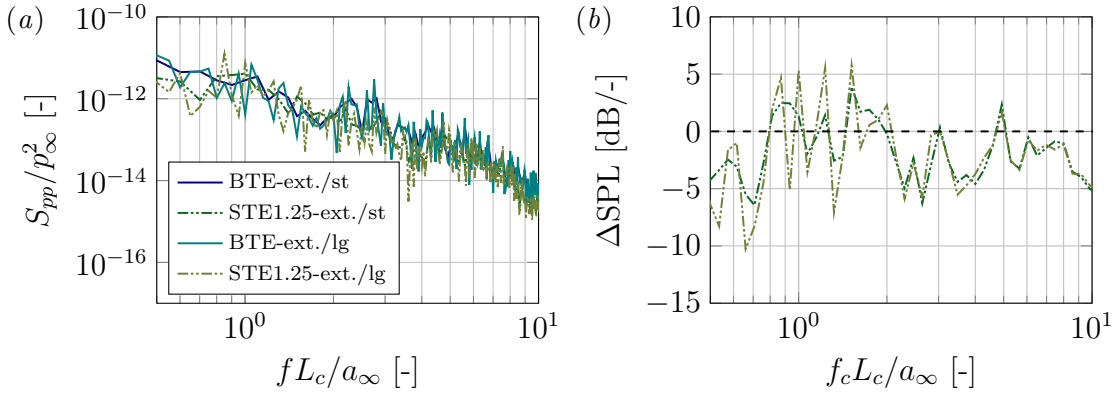

Figure A.35: Comparison of two time signal lengths ($ta_\infty/L_c = 10$ and 20) in terms of PSD of pressure fluctuations over a narrow circular arc $80^\circ \leq \theta \leq 100^\circ$ of a radius of $R/L_c = 100$ centred at the TE of the BTE case $(x, y, z)/L_c$=(1,0,0): (a) the individual PSDs and (b) the relative difference of the STE1.25 case to the baseline in decibels over one-tenth octave bands.

structures and consequently lower frequency content. Hence, an expanded span length study would be in the interest of many and may constitute a future subject of research. However, taking into account the available computational resources, the present study could not have presented so many high-fidelity simulations by running all cases with an extended span length due to the increased cost. It is also worth mentioning here that even if the span extent may have an impact on the generated far-field sound, the capability of the method exposed in this paper is unchanged as long as the same source is used for FW-H and Amiet's calculations.

The influence of the length of the extracted time signal is also investigated in the present section. After reaching steady-state, the extended span case is initially run for a period of $ta_\infty/L_c = 10$ and run again for a further 10 time units to obtain an overall extraction period of 20 time-units. Fig. A.35 compares BTE and STE1.25 cases for both 10 time-units and 20 time-units signals which are respectively referred to as "st" and "lg" for "short" and "long". As expected the longer time signal provides a more detailed spectrum in the low-frequency range. However, the results obtained with the shorter time signal are sufficiently accurate to characterise the sound in this frequency range.

Appendix B. Investigation of the local peaks in FW-H results

This appendix aims to explain the presence of peaks in the FW-H results (e.g. Fig. 14). These peaks are presumably due to the difference existing between the two approaches: Amiet's model is purely based on the wall pressure fluctuations information in the vicinity of the trailing edge whereas FW-H accounts for all the information over the aerofoil surface from leading to trailing edge. In particular, FW-H takes into account the contributions from the laminar-to-turbulent transition occuring at $x/L_c \simeq 0.5$. Fig. A.36 shows a comparison of three different frequencies in terms of wall pressure fluctuations over the suction side of the JK10-BTE case from transition to trailing edge. The magnitude distribution is represented by the PSD in log scale (Fig. A.36a) and the phase information is

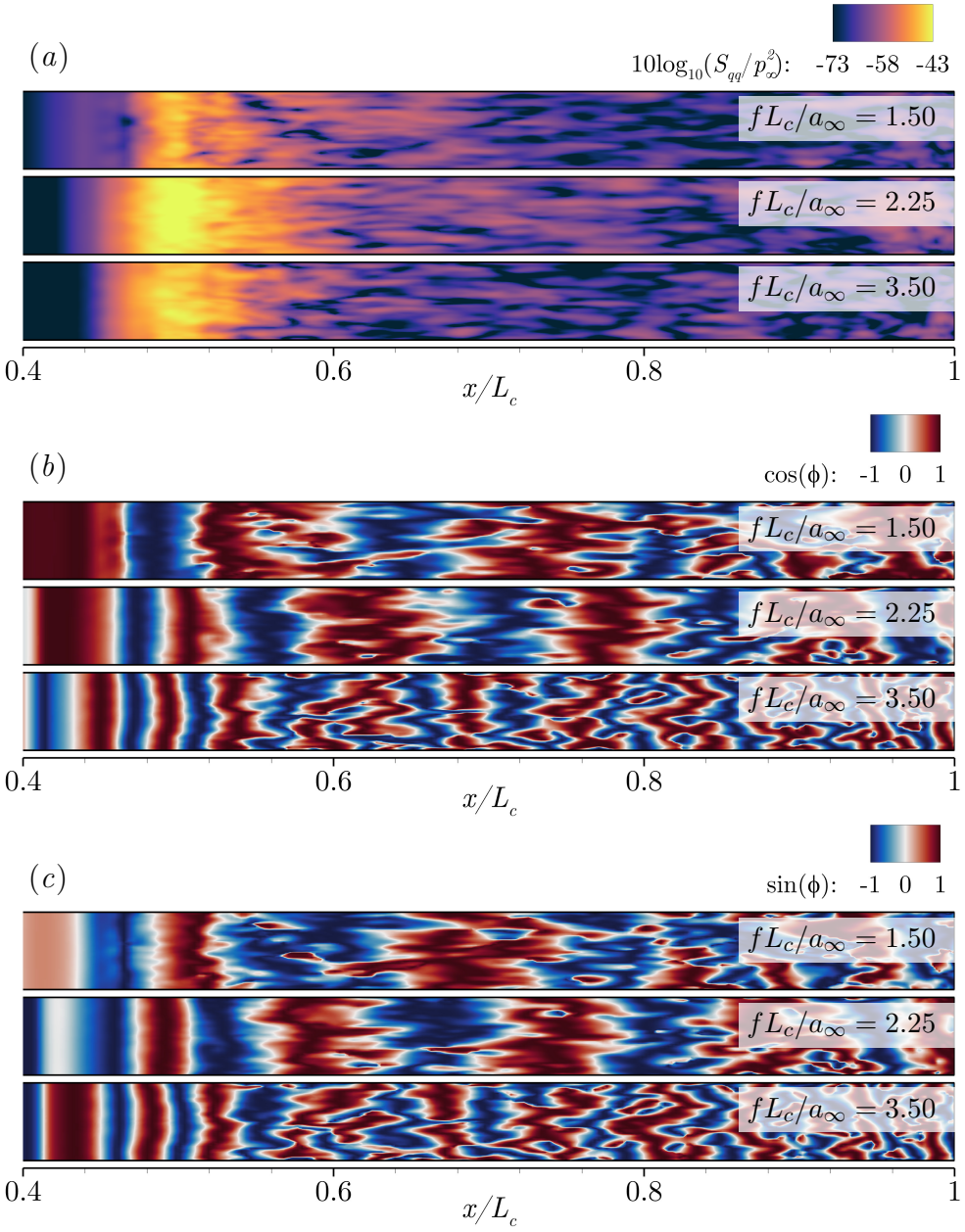

Figure A.36: Wall pressure fluctuations distribution on the suction side of the JK10-BTE case: (a) the PSD in log scale; the normalised (b) real and (c) imaginary parts of the Fourier transform.

displayed by the normalised real and imaginary parts, $\cos(\phi)$ and $\sin(\phi)$ respectively (Fig. A.36b,c). The frequencies showed in the figure are selected to illustrate the point with respect to Fig. 14. Thus, $fL_c/a_\infty = 1.5$ lies before the first main peak, $fL_c/a_\infty = 2.25$ lies in the peak and $fL_c/a_\infty = 3.5$ lies after it. A seen in Fig. A.36, the PSD maps show an increased intensity of the wall pressure fluctuations at $fL_c/a_\infty = 2.25$ compared to the two others. Furthermore, the phase distribution shows that, at this frequency, the pattern is more coherent which may lead to constructive interferences in the far-field. In summary, it is likely that the peaks in FW-H predictions result from the transition region. However, these peaks are weak compared to actual tonal noise [54] and therefore, they do not alter the broadband character of the signal. Furthermore, the authors did not find any correspondence between the observed peaks and the frequencies predicted by Arbey & Bataille's formula [55] confirming that the present spikes do not come from aerofoil tonal noise.

References

[1] T. F. Brooks, D. S. Pope, M. A. Marcolini, Airfoil self-noise and prediction, Technical Report NASA-RP-1218, National Aeronautics and Space Administration, 1989.

[2] S. Oerlemans, P. Sijtsma, B. Méndez López, Location and quantification of noise sources on a wind turbine, J. Sound Vib. 299 (2007) 869–883.

[3] R. K. Amiet, Acoustic radiation from an airfoil in a turbulent stream, J. Sound Vib. 41 (1975) 407–420.

[4] R. K. Amiet, Noise due to turbulent flow past a trailing edge, J. Sound Vib. 47 (1976) 387–393.

[5] M. Roger, S. Moreau, Back-scattering correction and further extensions of Amiet's trailing-edge noise model. Part I: theory, J. Sound Vib. 286 (2005) 477–506.

[6] F. Bertagnolio, Trailing Edge Noise Model Applied to Wind Turbine Airfoils, Technical Report 1633, RISO National Laboratory, Technical University of Denmark, 2008.

[7] S. Moreau, M. Roger, Back-scattering correction and further extensions of Amiet's trailing-edge noise model. Part II: Application, J. Sound Vib. 323 (2009) 397–425.

[8] Y. Rozenberg, S. Moreau, M. Henner, S. C. Morris, Fan blade trailing-edge noise prediction using RANS simulations, in: 16th AIAA/CEAS Aeroacoust. Conf., 2010, pp. 1–15.

[9] M. Kamruzzaman, A. Herrig, T. Lutz, W. Würz, E. Krämer, S. Wagner, Comprehensive evaluation and assessment of trailing edge noise prediction based on dedicated measurements, Noise Control Eng. J. 59 (2011) 54–67.

[10] M. Kamruzzaman, D. Bekiropoulos, A. Wolf, T. Lutz, E. Krämer, Rnoise: A RANS based airfoil trailing-edge noise prediction model, in: 20th AIAA/CEAS Aeroacoust. Conf., 2014, pp. 1–22.

[11] A. S. H. Lau, J. W. Kim, J. Hurault, T. Vronsky, P. F. Joseph, Aerofoil trailing-edge noise prediction models for wind turbine applications, Wind Energy 20 (2017) 1727–1752.

[12] Y. C. Küçükosman, J. Christophe, C. Schram, Trailing edge noise prediction based on wall pressure spectrum models for NACA0012 airfoil, J. Wind Eng. Ind. Aerodyn. 175 (2018) 305–316.

[13] T. F. Brooks, T. H. Hodgson, Trailing edge noise prediction from measured surface pressures, J. Sound Vib. 78 (1981) 69–117.

[14] S. Lee, J. G. Shum, Validation of an Empirical Wall Pressure Spectrum Model for Airfoil Trailing Edge Noise Predictions, in: 24th AIAA/CEAS Aeroacoust. Conf., 2018, pp. 1–10.

[15] J. Winkler, H. Wu, S. Moreau, T. Carolus, R. D. Sandberg, Trailing-edge broadband noise prediction of an airfoil with boundary-layer tripping, J. Sound Vib. 482 (2020) 1–25.

[16] R. D. Sandberg, N. D. Sandham, Direct numerical simulation of turbulent flow past a trailing edge and the associated noise generation, J. Fluid Mech. 596 (2008) 353–385.

[17] X. Gloerfelt, T. Le Garrec, Trailing edge noise from an isolated airfoil at a high Reynolds number, 15th AIAA/CEAS Aeroacoust. Conf. (2009) 1–26.

[18] M. Azarpeyvand, M. Gruber, P. F. Joseph, An analytical investigation of trailing edge noise reduction using novel serrations, in: 19th AIAA/CEAS Aeroacoust. Conf., 2013, pp. 1–17.

[19] T. Dassen, R. Parchen, J. Bruggeman, F. Hagg, Results of a wind tunnel study on the reduction of airfoil self-noise by the application of serrated blade trailing edges, in: Europ. Union Wind Energy Conf. and Exhibit., 1996, pp. 800–803.

[20] S. Oerlemans, M. Fisher, T. Maeder, K. Kögler, Reduction of Wind Turbine Noise Using Optimized Airfoils and Trailing-Edge Serrations, AIAA Journal 47 (2009) 1470–1481.

[21] M. Gruber, P. F. Joseph, T. P. Chong, On the mechanisms of serrated airfoil trailing edge noise reduction, in: 17th AIAA/CEAS Aeroacoust. Conf., 2011, pp. 1–23.

[22] D. J. Moreau, C. J. Doolan, Noise-Reduction Mechanism of a Flat-Plate Serrated Trailing Edge, AIAA Journal 51 (2013) 2513–2522.

[23] C. Arce León, D. Ragni, S. Pröbsting, F. Scarano, J. Madsen, Flow topology and acoustic emissions of trailing edge serrations at incidence, Exp. Fluids 57 (2016) 1–17.

[24] C. Arce León, R. Merino-Martínez, D. Ragni, F. Avallone, M. Snellen, Boundary layer characterization and acoustic measurements of flow-aligned trailing edge serrations, Exp. Fluids 57 (2016) 1–22.

[25] C. Arce León, R. Merino-Martínez, D. Ragni, F. Avallone, F. Scarano, S. Pröbsting, M. Snellen, D. G. Simons, J. Madsen, Effect of trailing edge serration-flow misalignment on airfoil noise emissions, J. Sound Vib. 405 (2017) 19–33.

[26] F. Avallone, S. Pröbsting, D. Ragni, Three-dimensional flow field over a trailing-edge serration and implications on broadband noise, Phys. Fluids 28 (2016) 1–20.

[27] T. P. Chong, A. Vathylakis, On the aeroacoustic and flow structures developed on a flat plate with a serrated sawtooth trailing edge, J. Sound Vib. 354 (2015) 65–90.

[28] L. E. Jones, R. D. Sandberg, Acoustic and hydrodynamic analysis of the flow around an aerofoil with trailing-edge serrations, J. Fluid Mech. 706 (2012) 295–322.

[29] F. Avallone, W. C. P. van der Velden, D. Ragni, D. Casalino, Noise reduction mechanisms of sawtooth and combed-sawtooth trailing-edge serrations, J. Fluid Mech. 848 (2018) 560–591.

[30] A. S. H. Lau, X. Huang, The control of aerodynamic sound due to boundary layer pressure gust scattering by trailing edge serrations, J. Sound Vib. 432 (2018) 133–154.

[31] M. S. Howe, Noise produced by a sawtooth trailing edge, The Journal of the Acoustical Society of America 90 (1991) 482–487.

[32] B. Lyu, M. Azarpeyvand, S. Sinayoko, Prediction of noise from serrated trailing edges, J. Fluid Mech. 793 (2016) 556–588.

[33] L. J. Ayton, Analytic solution for aerodynamic noise generated by plates with spanwise-varying trailing edges, J. Fluid Mech. 849 (2018) 448–466.

[34] B. Lyu, L. J. Ayton, Rapid noise prediction models for serrated leading and trailing edges, J. Sound Vib. 469 (2019) 1–13.

[35] J. E. Ffowcs Williams, D. L. Hawkings, Sound generation by turbulence and surfaces in arbitrary motion, Philosophical Transactions of the Royal Society of London, Series A, Mathematical and Physical Sciences 264 (1969) 321–342.

[36] D. J. Garmann, M. R. Visbal, P. D. Orkwis, Comparative study of implicit and subgrid-scale model large-eddy simulation techniques for low-Reynolds number airfoil applications, Int. J. Numer. Meth. Fl. 71 (2013) 1546–1565.

[37] F. M. White, Viscous fluid flows, McGraw-Hill, 1991.

[38] J. W. Kim, Optimised boundary compact finite difference schemes for computational aeroacoustics, J. Comput. Phys. 225 (2007) 995–1019.

[39] J. W. Kim, High-order compact filters with variable cut-off wavenumber and stable boundary treatment, Comput. Fluids 39 (2010) 1168–1182.

[40] J. W. Kim, Quasi-disjoint pentadiagonal matrix systems for the parallelization of compact finite-difference schemes and filters, J. Comput. Phys. 241 (2013) 168–194.

[41] M. Drela, XFOIL: An analysis and design system for low Reynolds number airfoils, Technical Report, MIT Dept. of Aeronautics and Astronautics, 1989.

[42] N. J. Georgiadis, D. P. Rizzetta, C. Fureby, Large-Eddy Simulation: Current Capabilities, Recommended Practices, and Future Research, AIAA J. 48 (2010) 1772–1784.

[43] S. I. Chernyshenko, M. F. Baig, The mechanism of streak formation in near-wall turbulence, J. Fluid Mech. 544 (2005) 99–131.

[44] J. W. Kim, D. J. Lee, Generalized characteristic boundary conditions for computational aeroacoustics, AIAA J. 38 (2000) 2040–2049.

[45] J. W. Kim, A. S. H. Lau, N. D. Sandham, CAA boundary conditions for airfoil noise due to high-frequency gusts, Procedia Eng. 6 (2010) 244–253.

[46] J. W. Kim, A. S. H. Lau, N. D. Sandham, Proposed Boundary Conditions for Gust-Airfoil Interaction Noise, AIAA J. 48 (2010) 2705–2710.

[47] F. Farassat, Derivation of Formulations 1 and 1A of Farassat, Technical Report March, NASA, 2007.

[48] J. M. Turner, J. W. Kim, Effect of spanwise domain size on direct numerical simulations of airfoil noise during flow separation and stall, Physics of Fluids 32 (2020) 1–15.

[49] M. E. Goldstein, Aeroacoustics, McGraw-Hill, 1976.

[50] R. D. Sandberg, N. D. Sandham, P. F. Joseph, Direct numerical simulations of trailing-edge noise generated by boundary-layer instabilities, J. Sound Vib. 304 (2007) 677–690.

[51] P. D. Lysak, Modeling the Wall Pressure Spectrum in Turbulent Pipe Flows, J. Fluids Eng. 128 (2006) 216–222.

[52] G. M. Corcos, The structure of the turbulent pressure field in boundary-layer flows, J. Fluid Mech. 18 (1963) 353–378.

[53] M. Gruber, P. F. Joseph, T. P. Chong, Experimental Investigation of Airfoil Self Noise and Turbulent Wake Reduction by the use of Trailing Edge Serrations, in: 16th AIAA/CEAS Aeroacoustics Conference, AIAA, 2010, pp. 1–23.

[54] M. B. R. Gelot, J. W. Kim, Effect of serrated trailing edges on aerofoil tonal noise, J. Fluid Mech. 904 (2020) 1–18.

[55] H. Arbey, J. Bataille, Noise generated by airfoil profiles placed in a uniform laminar flow, J. Fluid Mech. 134 (1983) 33–47.